Experimental characterization, machine learning analysis and computational modelling of the high effective inhibition of copper corrosion by 5-(4-Pyridyl)-1,3,4-oxadiazole-2-thiol in saline environment

Simona Varvara[1,*], Camelia Berghian-Grosan[2,*], Roxana Bostan[1], Raluca Lucacel Ciceo[3], Zohreh Salarvand[4], Milad Talebian[5], Keyvan Raeissi[5], Javier Izquierdo[6,7], Ricardo M. Souto[6,7]

[1] Department of Cadastre, Civil Engineering and Environmental Engineering, "1 Decembrie 1918" University of Alba Iulia, 15-17 Unirii St., 510009 Alba-Iulia, Romania

[2] National Institute for Research and Development of Isotopic and Molecular Technologies, Donat 67-103, 400293 Cluj-Napoca, Romania

[3] Faculty of Physics, Babes-Bolyai University, Cluj-Napoca, Romania. Interdisciplinary Research Institute on Bio-Nano-Science, Babes-Bolyai University, Cluj-Napoca, Romania

[4] Department of Chemistry, Chemistry and Petrochemistry Research Center, Standard Research Institute (SRI), Karaj 31747-34563, Iran

[5] Department of Materials Engineering, Isfahan University of Technology, Isfahan 84156-83111, Iran

[6] Department of Chemistry, Universidad de La Laguna, P.O. Box 456, E-38200, La Laguna, Tenerife, Spain

[7] Institute of Materials and Nanotechnology, Universidad de La Laguna, P.O. Box 456, E-38200 La Laguna (Tenerife), Spain

Abstract

An oxadiazole derivative with functional groups favouring its adsorption on copper surface, namely 5-(4-Pyridyl)-1,3,4-oxadiazole-2-thiol, has been explored as potential inhibitor of copper corrosion in 3.5 wt.% NaCl. Electrochemical evaluation by electrochemical impedance spectroscopy, potentiodynamic polarization and SVET reveals inhibition efficiencies exceeding 99%. Surface microscopy inspection and spectroscopic analysis by Raman, SEM-EDX and XPS highlight the formation of a compact barrier film responsible for long-lasting protection, that is mainly composed of the organic molecules. Machine Learning algorithms used in combination with Raman spectroscopy data were used successfully for the first time in corrosion studies to allow discrimination between corroded and inhibitor-protected metal surfaces. Quantum Chemistry calculations in aqueous solution and Molecular Dynamic studies predict a strong interaction between copper and the thiolate group and an extensive coverage of the metal surface, responsible for the excellent protection against corrosion.

Keywords

1. Introduction

Copper is one of the most important non-ferrous structural materials exhibiting excellent thermal and electrical conductivities, mechanical workability and relatively noble properties [1], so it is extensively used in a wide range of industrial fields such as electronics, automotive, marine, construction, pipeline and manufacturing industries [2,3]. Although copper exhibits good corrosion resistance under normal conditions, it is subjected to severe degradation when exposed to aqueous environments containing high chloride concentrations. Therefore, considerable effort has been devoted to controlling copper corrosion by applying various protection strategies [4], such as surface passivation, use of corrosion inhibitors, and surface modification using either self-assembling methods or application of coatings.

The use of corrosion inhibitors is one of the most effective, practical and economical methods of protecting copper against corrosion [3]. A large number of organic compounds have been synthesized, including azole derivatives [5-12], amines [13-15], Schiff bases [16-17], quinolines [18,19], and amino acids [20-22], and reported as effective corrosion inhibitors for copper in chloride-containing solutions. The effectiveness of these organic inhibitors is usually explained by their ability to adsorb on the copper surface through heteroatoms (N, P, O and S), conjugated double bonds, or aromatic rings with delocalised electrons in their molecular structures, forming barrier-type films which isolate the metal from the aggressive environment and prevent its corrosion.

Oxadiazole derivatives represent a class of heterocyclic compounds belonging to the azole family, which have an abundance of π-electrons and unshared electron pairs on the nitrogen and oxygen atoms which can interact with d-orbitals of metals to produce protective films on the surface [23]. Many oxadiazole derivatives have low toxicity [24] and a broad spectrum of biological activities [25-27], including antioxidant and antimicrobial activities.

A detailed review of the literature revealed that 1,3,4-oxadiazole derivatives have been recognised as excellent corrosion inhibitors for steels in various acid electrolytes [23,28-34]. However, much less attention has been paid to the use of substituted 1,3,4-oxadiazole compounds for the protection of the copper-based materials against corrosion [35,36]. Rochdi et al. [37] reported the anticorrosive properties of 2,5-bis(n-methylphenyl)-1,3,4-oxadiazole with ($n = 2,3,4$) on brass corrosion and scale formation in simulated cooling water. The highest inhibitory efficiency of about 91% was observed in the presence of 2,5-bis(3-methylphenyl)-1,3,4-

oxadiazole. Chadrasekaran et al. [36] also studied the inhibitory efficiency of four 1,3,4-oxadiazole derivatives, namely 2,5-diphenyl-1,3,4-oxadiazole, 2-amino-5-(4-methoxyphenyl)-1,3,4-oxadiazole, 2,5-bis(4-diethylaminophenyl)-1,3,4-oxadiazole, and 2,5-bis(4-aminophenyl)-1,3,4-oxadiazole on the corrosion of a copper-nickel alloy in natural seawater. Their results showed that these compounds are able to prevent the dissolution of nickel to a greater extent compared to copper. At their optimum concentrations (*i.e.*, 10^{-3} M), the maximum inhibition efficiencies reached the range 88-93%. In contrast, Raj and Rajendran [35] investigated four substituted 1,3,4-oxadiazoles as brass corrosion inhibitors in natural seawater and found their effectiveness to be quite poor. A correlation between the molecular structure of the compounds and their inhibition capacity was also proposed. Finally, certain heterocyclic compounds of 5-substituted-1,3,4-oxadiazole-2-thiols have been shown to be effective inhibitors for the prevention of nickel corrosion [38].

The present work aims to demonstrate the excellent inhibiting properties against copper corrosion of a substituted 1,3,4-oxadiazole, namely 5-(4-pyridyl)-1,3,4-oxadiazole-2-thiol (PyODT) in 3.5 wt.% NaCl aqueous solution. The choice of this compound was based mainly on its molecular structure (see Figure 1), that includes several functional groups, which can promote the adsorption of this compound on the surface of copper, namely the presence of a sulphur heteroatom from the thiol group, heteroatoms (N and O) in the 1,3,4-oxadiazole core, and the nitrogen atom with its lone sp^2 electron pair and the aromatic ring from the pyridyl group. Previous studies have shown that PyODT spontaneously adsorbs on gold, forming self-assembled monolayers through sulphur-gold interactions [39]. To the authors knowledge, no study devoted to the characterisation of PyODT anticorrosive properties has been reported to date.

The inhibitory efficiency of 5-(4-pyridyl)-1,3,4-oxadiazole-2-thiol on copper corrosion in aqueous NaCl environment was evaluated using a multiscale combination of electrochemical techniques, *i.e.* potentiodynamic polarization curves, electrochemical impedance spectroscopy (EIS) and the scanning vibrating electrode technique (SVET) to characterize both the inhibitor efficiency and the degree of homogeneity achieved by the surface layers formed on copper. The influence of inhibitor concentration and immersion time was investigated. The morphology of the copper surface was characterized by scanning electron microscopy (SEM), while various spectrometric and surface analytical techniques, such as X-ray dispersive energy spectrometry (EDX), Raman and X-ray-photoelectron spectroscopy (XPS), were used to collect information on

the adsorption of the inhibitor and the nature of the products formed on the surface of copper during the immersion tests.

In addition, a machine learning method based on the Raman data obtained by analyzing the copper surface after its immersion at different times in the blank and PyODT-containing solutions was applied to follow the evolution of the inhibitor film adsorbed on the metal, in correlation with the inhibitor concentration and the exposure time. The combination of Raman spectroscopy data and Machine Learning algorithms has already been reported [40,41] as a prospective tool capable of identifying adulterations in foods and beverages and for biological detection, in forensic and medical diagnostics as well as materials analysis, because of its power to detect patterns in complex data sets. However, this is the first time that Machine Learning algorithms have been used in corrosion studies to distinguish between Raman profiles of corroded and inhibitor-protected metal samples. Finally, quantum chemical (QC) calculations and molecular dynamics (MD) simulations were applied to discern the type of interaction established between the inhibitor molecules and the copper surface.

2. Experimental

2.1. Reagents and materials

The corrosive test electrolyte was a 3.5 wt.% NaCl aqueous solution (pH=5.5) prepared from analytical grade reagent (Merck, Darmstadt, Germany) and distilled water. The organic compound tested as a corrosion inhibitor was 5-(4-pyridyl)-1,3,4-oxadiazole-2-thiol (PyODT) purchased from Sigma Aldrich (97%; St. Louis, MO, USA); its structural formula is shown in Figure 1. The electrolytes containing the inhibitor were prepared by dissolving appropriate weighted amounts of 5-(4-pyridyl)-1,3,4-oxadiazole-2-thiol in a mixture of 3.5% NaCl solution and ethanol (90:10 v/v). The concentrations of PyODT used were 0.25, 0.5, 1 and 1.5 mM.

2.2. Electrochemical characterization

The corrosion tests were carried out using working electrodes made up of a pure copper cylinder embedded in an epoxy resin (Epoxycure^{TM}, Buhler, Uzwil, Switzerland). Areas of 1 cm^2 and 0.28 cm^2 were exposed to the test solution for potentiodynamic polarization and the electrochemical impedance measurements, respectively. The counter electrode was a large platinum grid and an Ag/AgCl/KCl$_{sat}$ electrode was used as reference. Before the corrosion tests,

the working electrode was mechanically abraded under a stream of water with 1200 and 4000 grade silicon carbide papers, then polished with 0.3 µm alumina slurry to obtain a mirror-like surface. Finally, the copper electrode was degreased with ethanol, rinsed thoroughly with distilled water, dried and immediately introduced in the corrosive solution.

Conventional electrochemical experiments were performed in a three-electrode cell configuration, using a Model 2273 PAR potentiostat (Ametek, Berwyn, PA, USA). Before each experiment, the copper electrode was left at the open circuit potential (OCP) for 1 h in the test solution without or with PyODT. Potentiodynamic polarization curves were recorded at a constant scan rate of 10 mV min^{-1} over a potential range of ±250 mV *vs.* OCP, from the cathodic to the anodic direction. A new sample was employed each time to record a polarization curve. Electrochemical impedance spectra (EIS) were acquired at OCP in the frequency range 10 kHz to 10 mHz with 5 points per decade and with an AC voltage amplitude of ±10 mV. To evaluate the stability over time of the PyODT protective film formed on the surface of copper, EIS measurements were carried out at various immersion times up to 168 h. The impedance results were interpreted on the basis of equivalent electrical circuits using the *ZSimpWin 3.21* software (Ametek, Berwyn, PA, USA).

2.3. Scanning vibrating electrode technique (SVET)

Copper foil of 1 mm thickness and 99.9% purity (Goodfellow, Cambridge, UK) was used for the SVET analysis of the inhibitory effect of PyODT. The metal was cut into strips of approximate dimensions of 1 mm × 2 mm, then embedded in insulating cold-curing Epofix resin (Struers, Ballerup, Denmark), resulting in a 3 cm diameter sample with a flat Cu surface exposed in the centre.

SVET measurements were performed using an Applicable Electronics equipment (New Haven, CT, USA) controlled by *Automated Scanning Electrode Technique* (ASET) software installed on a personal computer. A 2 cm long Pt-Ir probe, coated with an insulating layer of Parylene-C but for the 10 µm diameter point end, was used after electroplatinization in H_2PtCl_6 solution, to generate a spherical deposit of platinum black of 20 µm diameter at the tip [42]. The vibration frequencies of the probe were 310 Hz along the *X* axis and 70 Hz along the *Z* axis, both with an amplitude of 20 µm.

The scans were performed over the surface of copper at a height of 100 μm, that was established using the video imaging system supplied with the equipment. SVET measurements were performed in a naturally aerated 50 mM NaCl solution with and without 1.5 mM PyODT inhibitor at ambient temperature (20 ± 2 °C) for 4 h. A lower concentration of NaCl was selected for SVET measurements due to the increased noise sensed by SVET when high electrolyte concentrations compensate for ionic gradients arising from the corroding surfaces [42]. The sample was left unpolarized, effectively at its open circuit potential (OCP) in the test electrolyte.

2.4. SEM-EDX characterization

A JSM 5600 LV scanning electron microscope (SEM; JEOL, Akishima, Tokyo, Japan) was used in conjunction with an energy dispersive X-ray spectrometer (EDX; Oxford Instruments, Abingdon, UK) to characterize the surface of the copper samples after 24 h exposure to 3.5 wt.% NaCl solution in the absence and the presence of PyODT.

2.5. Raman spectroscopy

Raman spectra were obtained using a JASCO NRS-3300 (Easton, USA) equipped with a CCD detector (-69 °C) and a 785 nm diode laser excitation line. The laser was focused on the sample through a 100× objective (UMPLFL Olympus, Shinjuku, Tokyo, Japan). The Si peak (at 521 cm^{-1}) was used for the calibration procedure. Each sample was investigated at various points (minimum 6, maximum 20), depending on the homogeneity of the analysed surface. Each spectrum was collected with an exposure time of 60 s and a minimum of 3 accumulations. The Raman spectra were collected on the copper surface after exposure for various times (namely, 1, 6 and 24 h) in the test solution, in the absence and in the presence of PyODT.

JASCO Spectra Manager tools (Easton, USA) were employed for spectrum analysis. Before any processing of the Raman data, a selection was made of the frequency ranges between 130 and 1800 cm^{-1}. Then, each spectrum was subjected to baseline subtraction and [0,1] normalization. These pre-treatments were performed in *OriginPro 2017* (OriginLab, Northampton, MA, USA). The Raman data were used for both general Raman and Machine Learning studies.

2.6. X-ray photoelectron spectroscopy (XPS)

XPS measurements were performed on the copper samples (of area 1 cm^2) after 24 h of exposure to blank and PyODT-containing solutions, using a PHOIBOS 150 MCD (**S**PECS Surface Nano Analysis GmbH, Berlin, Germany). The instrument was equipped with a monochromatic Al Kα source (250 W, $h\nu$ = 1486.6 eV), a hemispherical analyser and a multichannel detector. The typical vacuum in the analysis chamber during measurements was on the order of 10^{-9}–10^{-10} mbar. Charge neutralization was used for all samples. The binding energy scale was charge-referenced to the C1s photoelectron peak at 284.6 eV. The survey spectra were acquired at a pass energy of 60 eV in the binding energy range of 0 to 1200 eV. High resolution spectra were obtained using an analyser pass energy of 20 eV. The position and the full width at half maximum of photoelectron peaks were estimated by spectra deconvolution with *Casa XPS* (Casa Software Ltd., Teignmouth, UK) assuming a Shirley type background. The experimental core level spectra were fitted using a GL30 line shape of Gaussian and Lorentzian functions.

2.7. Machine Learning (ML) studies

The Classification Learner application implemented in *MATLAB R2018b* (MathWorks, Natick, MA, USA) was used for Machine Learning (ML) studies on pre-treated Raman spectra of the samples. Before the ML investigation, a training set was created which contained, for each sample, a set of spectra (ranging from 5 to 15, depending on the homogeneity of the sample). Therefore, the trained data sets were created for 14 samples, namely: copper specimen – Cu, solid form of PyODT, film found on the copper surface after various immersion times in 3.5 wt.% NaCl solution both, in the absence (blank) (*i.e.,* Cu-blank-1h, Cu-blank-6h, Cu-blank-24h) and in the presence of PyODT at various concentrations (that is, Cu-PyODT-0.25mM-1h, Cu-PyODT-0.25mM-6h, Cu-PyODT-0.25mM-24h, Cu-PyODT-1mM-1h, Cu-PyODT-1mM-6h, Cu-PyODT-1mM-24h, Cu-PyODT-1.5mM-1h, Cu-PyODT-1.5mM-6h, and Cu-PyODT-1.5mM-24h). As result, a total number of 129 spectra were employed in this analysis. Based on these experimental data, the ML extracted the essential information and built a classification model. Other 38 Raman spectra, selected at random and guaranteeing the representativeness of each investigated film, were used for the generation of the test set. These testing data were employed to verify the prediction model obtained in the training set.

In this study in which Raman spectroscopy data and Machine Learning algorithms were combined to track the evolution of the film formed on the copper surface as a function of both, the

inhibitor concentration and the immersion time, five predictive modelling approaches have been used: decision trees [43], discriminant analysis [44], support vector machines (SVM) [45], nearest neighbour classifiers (KNN) [46], and ensemble classifiers [47].

2.8. Quantum chemical calculations (QC)

The QC calculations were performed by density functional theory (DFT) using the *Gaussian09* software package [48]. The geometrically optimized structure of the inhibitor was achieved in the gas phase using the DFT method at the unrestricted B3LYP 6-311++G(d,p) level of theory for all atoms. To study the effect of solvation on the molecular structure and chemical reaction, calculations were performed with the same method at the unrestricted B3LYP 6-311++G(d,p) level of theory in the presence of water as solvent, applying the polarizable conductor model (CPCM) based on the polarized continuum model (PCM) [49,50]. The DFT calculation consists of thiol-thione tautomerism by the intramigration reaction of a single proton. The QST2 calculation method was applied to study the reaction path for intramigration between the two optimized tautomers [51]. Key chemical indices such as the energies of the highest occupied molecular orbital (E_{HOMO}), and the energy of the lowest unoccupied molecular orbital (E_{LUMO}), the energy band gap (ΔE) between LUMO and HOMO, the dipole moment (μ), as well as the number of transferred electrons (ΔN) and the pK_a for the tautomeric thione and thiol isomers of the PyODT molecule.

2.9. Molecular dynamics simulation (MD)

MD simulation studies were performed using *Material Studio 6.0* software (Accelrys Inc., San Diego, CA, USA) to learn more about the adsorption of the inhibitor molecules on the metal surface at the molecular level. The MD simulations were carried out by taking single crystal Cu (111) surface (the most densely packed and therefore the most stable [52]) in a simulation box of dimensions 3.58 nm × 3.58 nm × 3.61 nm with periodic boundary conditions to model a representative part of the interface devoid of any arbitrary boundary effects. The appropriate surface was first cleaved from pure Cu crystal and relaxed by minimizing its energy using molecular mechanics. The surface area of Cu (111) was enlarged to fabricate an appropriate supercell, and to build a zero thickness vacuum slab above these surfaces. The chemical species included in the adsorption system were 200 H_2O, 2 Na^+, 2 Cl^- and 1 PyODT molecule in each case.

The system was constructed using the Amorphous Cell Program, and then the corrosion system was built by Layer Builder by placing the Amorphous Cell on the Cu (111) supercell. In addition, all layers of the supercell except the top layer were kept fixed. The MD simulations were performed at 298.0 K (controlled by the Andersen thermostat) under the NVT ensemble (*i.e.* the canonical ensemble), with a time step of 1.0 fs and a simulation time of 500 ps, by COMPASS (condensed-phase optimized molecular potentials for atomistic simulation studies) force field [53].

3. Results and discussion

3.1. Electrochemical characterization

3.1.1. Electrochemical impedance spectroscopy

The EIS measurements were performed at the corrosion potential spontaneously attained after various exposure times of copper to a 3.5% NaCl solution, in the absence and in the presence of PyODT. The first impedance measurement was made after a stabilization period of 1 h at 298 K. Long-term impedance tests of up to 168 h were aimed at evaluating the stability and corrosion resistance provided by the adsorption of the inhibitor on the copper surface.

Figure 2 shows typical examples of impedance diagrams recorded at different immersion times of the Cu corroding surface in the blank test electrolyte and in the presence of PyODT at various concentrations. Nyquist plots are characterised by a semi-circular appearance with two poorly separated capacitive loops over the entire frequency range studied. A diffusion tail at low frequencies was also observed in the impedance diagrams obtained in the blank solution and in the presence of PyODT at low concentrations ($\leq$ 0.5 mM). As stated previously [54], Warburg impedance could be attributed either to the diffusion process of soluble cuprous chloride complexes (*i.e.*, $CuCl_2^-$ and $CuCl_4^{2-}$) from the copper surface to the bulk solution or to the transport of dissolved oxygen toward the electrode. The occurrence of the diffusion process in the EIS spectra obtained at low PyODT concentrations could be due to reduced inhibitor adsorption, which is not able to form a dense and ordered barrier film on the copper surface. In contrast, at higher concentrations of PyODT (> 0.5 mM), the Warburg impedance disappears, and in Figure 2 a significant increase in semicircle diameters is readily seen, which is directly correlated with development of a highly protective inhibitor film on the metal [15,55,56]. In addition, the anticorrosive protection ability of PyODT at high concentrations is significantly improved during the exposure period. As for example, in the presence of 1.5 mM PyODT, a gradual increase in low

frequency impedance values, |Z|, with the immersion time could be readily noticed in Figure 3, while the corresponding maximum phase angles approach -90°. This behaviour confirms the efficient adsorption of the organic molecule on copper, which leads to better inhibition of the corrosion process.

Further information on the electrochemical processes that occur at the copper interface was obtained through the analysis of EIS spectra using the two equivalent electrical circuits [57] shown in Figure 4. Since the two capacitive loops appear like depressed semicircles in Figure 2, constant phase elements (CPE) were used instead of ideal capacitances to account for deviations caused by surface roughness, inhibitor adsorption, porosities, and other surface inhomogeneities [58]. In Figure 4, R_s represents the solution resistance; R_f corresponds to the resistance against the access of aggressive chloride ions through a surface film that is reinforced by the adsorption of the inhibitor; R_{ct} is the charge transfer resistance, while CPEf and CPEdl are associated with constant phase elements, respectively modelling film capacitance (C_f) and double layer capacitance (C_{dl}). Finally, W represents the Warburg element in the low frequency range, induced by the diffusion of soluble Cu species from the electrode surface to the bulk solution [54].

The impedance of CPE is described as follows:

$$Z = [Y(j\omega)^n]^{-1} \tag{1}$$

where $\omega = 2\pi f$ is the angular frequency, $j = (-1)^{1/2}$ is the imaginary unit, Y is the magnitude of the CPE, and n is a fitting parameter ($0 \leq n \leq 1$), which measures the deviation of the element of ideal capacitive behaviour (showing $n = 1$) [58-60]. For each R-CPE couple, the general equation:

$$C = (R^{1-n} Y)^{1/n} \tag{2}$$

was used to convert the Y parameters of the CPE elements into associated capacitances [61].

Table 1 presents the fitted parameters obtained at different immersion times for the corrosion of copper in the absence and in the presence of various concentrations of PyODT. Table 1 also lists the inhibition efficiency values, η_{Imp}, determined according to the following equation:

$$\eta_{Imp} (\%) = \frac{R_{ct} - R_{ct}^0}{R_{ct}} \cdot 100 \tag{3}$$

where R_{ct} and R_{ct}^0 are the charge transfer resistances in solutions with and without PyODT, respectively.

The fitted impedance plots represented by crosses are shown in Figures 2 and 3 with the experimental data represented by symbols. The good overlap between the calculated and experimental results confirms the validity of the proposed models. However, in some cases,

11

especially for long exposure times, it was difficult to unambiguously calculate the *R-C* parameters corresponding to the second time constant obtained in the presence of PyODT. To improve the fitting procedure, the n_{dl} values were kept at fixed values during the iterations. In the blank solution, the resistance of the film, R_f, gradually increases during the first 24 h of immersion, but beyond this period it begins to decrease and reaches rather low values at the end of the corrosion test (168 h). A similar variation was observed for the capacitance of the film, C_f (cf. Table 1). As explained previously [62], a thin and highly resistive oxide layer could slowly form on the surface of copper during the initial stages of immersion. By prolonging the metal exposure to the aggressive action of the Cl^- ions, this rather protective surface layer undergoes alteration, being replaced by a new thicker but less resistive oxide film. As expected, the charge transfer resistance, R_{ct}, progressively increases during the immersion time and reaches the highest value of 8.03 kΩ cm^2 at 24 h of exposure. Table 1 also shows a decrease over time in the double layer capacitance, C_{dl}. It reaches 12.33 µF cm^{-2} at 24 h of immersion. With longer exposure, the corrosion of copper proceeds faster, leading to a rougher surface, which explains the increase in C_{dl} values at the end of the experiments.

As shown in Table 1, the protective effect of PyODT on copper corrosion depends on both the inhibitor concentration and the exposure time. Therefore, at the lowest concentration (0.25 mM), PyODT somewhat hinders the copper corrosion process, but only in the first 4 hours of immersion (results not shown here). Then, the PyODT rather has an activating effect on the corrosion of copper, explained in view of the decreases in the pH of the solution caused by the addition of the inhibitor. There was also a weak protective effect on copper in the presence of 0.5 mM PyODT in the initial stages of the immersion (during the first 7 h), as R_f is slightly higher compared to the blank solution, while R_{ct} has similar values. The corresponding variations of C_f and C_{dl} confirm that at low concentrations PyODT cannot rapidly adsorb on the surface of copper and to form a stable and orderly barrier film. On the other hand, the inhibitory effect of 0.5 mM PyODT on copper corrosion becomes significant at about 8 h of exposure and gradually increases up to 48 h. The sharp decrease in the C_f values observed at 8 h exposure in the presence of 0.5 mM PyODT is correlated with a sudden thickening of the surface film formed on copper, which remains fairly constant throughout the remaining period of exposure. However, the nature and permeability of this barrier film against the aggressive Cl^- ions seem to change during corrosion tests [63]. Although the increasing trend in R_f values within 72 h of exposure may be related to a more

compact and resistive nature of the surface film, the electrolyte begins to penetrate through this film with prolonged exposure, decreasing its resistance. Consequently, a gradual acceleration of the corrosion process could be noted at the end of the experiments (168 h). The failure of PyODT at 0.5 mM concentration to provide lasting protection to copper is also confirmed by the significant decrease in R_{ct} values at 168 h, while the C_{dl} value increases relative to the blank solution. On the contrary, the protective film formed on the copper surface becomes more compact and stable when the concentration of inhibitor increases, as evidenced by the high values of the film resistances obtained in the presence of 1 mM and 1.5 mM PyODT (cf. Table 1). In addition, the R_f values gradually increase with the time of exposure to solutions containing high concentrations of PyODT and reach values of approximately 0.55-0.60 MΩ cm^2 at the end of experiments. These high R_f values indicate the presence of an extremely resistant adsorbed inhibitor film on the copper surface which greatly prevents the penetration of aggressive Cl$^-$ ions from the solution. This was confirmed by the results of the surface analysis presented below, which revealed the presence of nitrogen and sulphur atoms on the surface of copper.

As expected, a significant increase in charge transfer resistance, R_{ct}, was observed in solutions containing high concentrations of PyODT, while simultaneously the double layer capacitance values, C_{dl}, gradually decreased relative to the blank solution. The decrease in C_{dl} values correlates with the adsorption of PyODT on the copper surface, which leads to a smaller corroding area directly in contact with the aggressive solution. The results are also consistent with the low values of the n_{dl} coefficient, indicating the heterogeneity of the electrochemical processes at the active sites [54].

As shown in Table 1, the inhibition efficiency values increase significantly with increasing inhibitor concentration and immersion time. At the highest concentrations studied, PyODT exerts a significant anticorrosion effect on copper from the start of immersion, as evidenced by the high values of η_{Imp}, which respectively reach 92.8% and 93.3% in the presence of 1 mM and 1.5 mM PyODT. An important enhancement of inhibitory properties of PyODT was noted during prolonged exposures, when the η_{Imp} values exceeded 99%, confirming its excellent long-term protective action on copper corrosion.

3.1.2. Potentiodynamic polarization curves

The influence of PyODT on the polarization behaviour of copper in 3.5% NaCl solution was evaluated on the basis of polarization curves. The copper samples were left in the test solution for different periods of time, then the polarization curves were recorded from the cathodic to the anodic potentials ranges. Figure 5 shows the potentiodynamic polarization curves of copper in 3.5% NaCl solution without and with various concentrations of PyODT, recorded after immersion for 1 and 48 h, respectively.

The polarization behaviour of copper in the blank electrolyte is similar in the two immersion times and is in agreement with previously reported results [64]. Therefore, starting from the corrosion potential, E_{corr} the anodic current density increases steadily with the potential. The related process is the dissolution of copper into Cu^+, followed by the formation of a soluble $CuCl_2^-$ complex [65]. As the potential becomes more positive, in Figure 5 a region of currents decreasing to a minimum value can be noticed, due to the formation of an insoluble layer of CuCl on the surface of copper. This layer is not protective and further reacts with Cl^- ions forming the soluble $CuCl_2^-$ complex, which can either diffuse into the bulk solution or undergo further oxidation [65]. The cathodic reaction sustaining the corrosion process of copper is the reduction of molecular oxygen.

In the presence of PyODT, a displacement of the anodic and cathodic branches of the polarization curves towards lower current densities could be seen (Figure 5). This trend is more pronounced at high concentrations of the inhibitor and at prolonged duration of exposure. In particular, the current associated with the anodic dissolution reaction seems to be more inhibited than the cathodic one. There is also a gradual decrease in the anodic current peak corresponding to the formation of CuCl, while the concentration of PyODT increases. In fact, the anodic current peak disappears, and a broad current plateau can be seen in the polarization curves recorded at 48 h of copper exposure to solutions containing high concentrations of inhibitor (Figure 5b). Such passivation behaviour could be explained by a strong adsorptive interaction between PyODT molecules and copper, leading to the development of a compact inhibitory film on the surface, thus preventing the dissolution and migration of copper ions (associated with the Warburg element in EIS analysis), which provides remarkable inhibition of the corrosion process.

The electrochemical parameters such as the corrosion potential (E_{corr}), the corrosion current density (j_{corr}) and the anodic Tafel slope (β_a) determined from the polarization curves are listed in Table 2. The corrosion inhibition efficiency values (η_{Pol}) were also calculated using the equation:

$$\eta_{Pol} (\%) = \frac{j^0_{corr} - j_{corr}}{j^0_{corr}} \cdot 100 \qquad (4)$$

where j^0_{corr} and j_{corr} denote the corrosion current density values determined in the absence and presence of PyODT, respectively.

A definite trend could not be observed in the changes of the E_{corr} values obtained at 1 h exposure in the presence of different concentrations of organic inhibitor (see Table 2). On the contrary, there is a progressive displacement of the E_{corr} towards more noble values with a longer exposure. For example, the E_{corr} value is shifted in the anodic direction by +164 mV in the case of a solution containing 1.5 mM PyODT, relative to the blank electrolyte. Based on these results, it was assumed that PyODT acts as an effective mixed-type inhibitor, with a predominant inhibitory effect on the anodic reaction. However, over long immersion times PyODT most likely behaves as an anodic inhibitor, especially at high concentrations. The significant change in the anodic process is evidenced by the notable increase in the values of the anodic Tafel slope (cf. Table 2).

As expected, the values of j_{corr} gradually decrease in the presence of PyODT for all concentrations studied, both for short and long immersion times. The only exception was observed in the presence of 0.25 mM PyODT at 48 h of exposure, when an acceleration of the copper corrosion process was assumed based on the increased value of j_{corr}, compared to the blank solution. These results agree with the EIS and Raman spectroscopy data. As the inhibitor concentration increases, the inhibition efficiency of PyODT increases markedly and improves further at longer immersion time.

3.2. Surface analysis

3.2.1. SEM and EDX characterization

SEM images (Figure 6) and EDX analysis (Figure 7) were performed on copper samples after 24 h immersion in 3.5% NaCl solution, in the absence and presence of 1 mM PyODT. As shown in Figure 6b, the copper surface is covered with a thick layer of corrosion products after 24 h immersion in 3.5% NaCl solution. As expected, EDX analysis showed the presence of Cu, O, and Cl on the copper electrode (Figure 7a). This is consistent with the typical composition of the corrosion products formed on copper after exposure to a chloride-containing solution, consisting mainly of CuCl and Cu_2O compounds [65]. The traces of Si and Al detected on copper come from previous surface preparation steps which also generated the grinding scratches visible in Figure 6.

In the presence of PyODT, the copper surface appears to be flat and covered with a thin film of organic inhibitor (see insert in Figure 6c). The presence of molecules of the organic inhibitor adsorbed on the copper surface is confirmed by the nitrogen and sulphur atoms detected in the EDX spectra (Figure 7b). However, some small traces of corrosion products are still present on the surface of copper exposed for 24 h to a solution containing 1 mM PyODT, but this was expected considering that its inhibitory efficiency is slightly less than 100%.

3.2.2. Raman characterization and Machine Learning studies

Raman spectroscopy was used to study the interaction of the PyODT molecule with the copper surface and to assess the temporal evolution of the inhibitor film during immersion in the corrosive solution. Figure 8a shows the Raman spectra of an untreated copper sample and the copper surface after 1 and 24 h immersion in 3.5 wt.% NaCl. Three peaks were observed for the copper sample at 275, 528 and 613 cm^{-1}, which could be assigned to the vibration of the Cu-O bond of Cu_2O and CuO species that existed on the surface of copper [66,67]. The Raman study of the Cu surface after different immersion times in a 3.5 wt.% NaCl solution did not allow a detailed survey of the evolution of corrosion over time. However, these spectra show changes in the intensities of two bands, namely an increase in the peak at 275 cm^{-1} and a decrease in that at 613 cm^{-1}, as well as slight shifts in these to 279 and 605 cm^{-1}, respectively. These changes could be associated with the appearance of corrosion on the copper surface and the formation of Cu-Cl (chloride related species) [68].

The Raman spectra of the copper surface before and after immersion in 3.5 wt.% NaCl solution in the absence and in the presence of different concentrations of PyODT are shown in Figure 8b and Figure 9. For comparison purposes, the spectrum of PyODT in the solid state is also presented in Figure 8b. As revealed in Figure 8b and Figure 9, the bands corresponding to the inhibitor molecule are visible in all Raman spectra, regardless of their concentration in the electrolyte or the immersion time of the electrode. However, Figure 8b shows some important differences between the Raman patterns of the copper surface exposed for 24 h to electrolytes containing different concentrations of PyODT. Unlike the copper sample treated with low concentrations of inhibitor, in the presence of 1.5 mM PyODT, a clear Raman profile of the inhibitor film is visible even in the low wavenumber region (that is, the region for the bands related to the copper oxides, namely 200-800 cm^{-1}), which proves that the adsorbed organic film is more

uniform and compact and should therefore offer better protection to the copper surface. These observations are in agreement with the electrochemical results, which also showed an improved anticorrosion effect of PyODT at the concentration of 1.5 mM.

To better understand the adsorption behavior of PyODT on the copper surface, a comparison was also made between the frequencies of the solid state and the chemisorbed states of PyODT (see Figure 8b). At neutral pH, the thiol form is predicted to be predominant, and can be further ionized in aqueous solution as indicated in equation (5):

$$\text{thione} \quad \leftrightarrow \quad \text{thiol} \quad \leftrightarrow \quad \text{thiolate ion} \qquad (5)$$
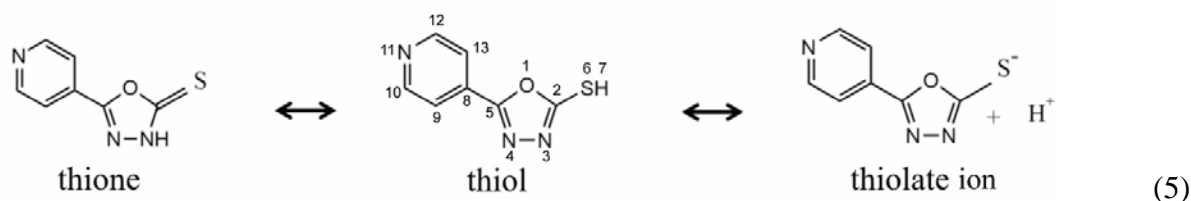
The Raman spectrum of PyODT indicates the thione form as the major tautomer existing in the solid (powder) state (*i.e.,* the band at 1074 cm^{-1} can be assigned to the stretching mode of the N-protonated form of the oxadiazole group [69]), in accordance with the crystal structure of PyODT obtained by an X-ray diffraction study [70]. This band disappeared after adsorption of PyODT on the copper substrate and a new band was observed at 991 cm^{-1}. This peak could be attributed to the C-S stretching vibration ν(C-S), which is observed at 989 cm^{-1} for similar compounds after adsorption on gold [71]. Moreover, a shift of the other two peaks, 953 and 1010 cm^{-1}, could be also noticed in the region from 950 to 1100 cm^{-1} after the adsorption of PyODT on copper. The first peak is attributed to 12 vibration modes of the pyridyl group, while the second to ν(COC) and ν(NN) of the oxadiazole ring [69].

Another significant variation appears in the Raman spectra of the two forms of PyODT in the range 1400–1620 cm^{-1} (see Figure 8b). Two main peaks were observed for the solid state of PyODT at 1534 and 1616 cm^{-1}, which could be attributed to the superposition of the C=N stretching vibration ν(C=N) of the oxadiazole ring, and to the 8b and 8a vibration modes of the pyridyl moiety, respectively [69]. In the adsorbed form of PyODT, an intense peak appeared at about 1422 cm^{-1}. This can be attributed to ν(C=N) of the oxadiazole ring, while those at 1542, 1572 and 1608 cm^{-1} to a superposition between the ν(C=N) vibration of the oxadiazole and the 8b, 9b or 8a vibration modes of the pyridyl ring [69].

Altogether, these results indicate that the tautomer containing unprotonated nitrogen atoms, both in the oxadiazole group and in the pyridyl ring, is the most suitable structure for the chemisorbed PyODT film layer.

In addition, the evolution of the inhibitory film on the copper surface in correlation with the PyODT concentration and the immersion time was investigated by considering the Raman spectra and Machine Learning algorithms. To achieve this, Raman surveys were carried out in different points on each sample; some of the Raman data were used for the training set, while others were used for the assembling of a test group (see Experimental Section 2.7). Raman data from the training set contributed to model prediction, while spectra from the test group were used for validation of the prediction model (see Figure 10 and Table 3). The objective was to study the degree of similarity between the spectra collected at different points and to determine whether they can be associated with specific inhibitor concentrations or immersion times. Therefore, the model was trained using Raman data recorded at different points and at various stages of the copper surface (*i.e.* untreated Cu, Cu exposed for different periods of time (1 h, 6 h, 24 h) to electrolytes without (blank sample) and with the addition of various PyODT concentrations, 0.25 mM, 1 mM and 1.5 mM; see Figure 9). Various Machine Learning algorithms have been used for this purpose (see Experimental section); the best accuracy of 81.6% was obtained when the Linear Discriminant algorithm with full covariance structure and five-fold cross-validation was applied to the training set. This accuracy result is mainly due to the incorrect classification of some samples of Cu-PyODT-1.5mM recorded at 1 h (3 of 6 samples) and 24 h (5 of 10 samples), which appear assigned to the other two concentration groups (0.25 and 1 mM). The situation is not uncommon since at the electrode surface different types/organizations of the organic layers could be found at such a high concentration. For the other investigated classes, the results reveiled either an incorrect assignment within each class for Cu-PyODT-0.25mM, Cu-PyODT-1mM and Cu-blank or a true prediction, with two exceptions (1 sample of Cu-PyODT-0.25mM 1h and respectively 24h) for Cu, PyODT and Cu-PyODT-0.25mM groups (see Figure 10).

To assess the performance of the model, the outcomes obtained by applying the prediction model on the test data set were analysed and presented in Table 3. They revealed only one incorrect assignment of the 38 investigated samples, in particular a Cu-blank-6h sample was assigned to the Cu-blank-24h one. No other incorrect assignments were found within or between the investigated classes (see Table 3), indicating that the method worked well in predicting the Raman profile types

of these classes. Thus, employing this model, it was possible to discriminate between the spectra of copper affected by corrosion and those achieving protection by the organic inhibitor.

3.2.3. XPS spectroscopy

In order to assess the transformations that occur on the surface of copper during the corrosion process, in the absence and in the presence of the organic inhibitor, an XPS study was also performed. In addition to Cu, it is worth mentioning the existence of the elements O, Na and Cl in the survey spectra recorded on the copper sample after 24 h of immersion in a 3.5 wt.% NaCl solution in the absence and in the presence of different concentrations of PyODT (see Figure 11), whereas N and S are present in the XPS spectra obtained on the copper surfaces treated with 1 and 1.5 mM PyODT (Figure 11). In addition, it was expected that the structure of the adsorbed layer would be determined by analysing the deconvoluted spectra of the major elements (*i.e.*, Cu, C, N, O, S, Cl) as shown in Figures 12-14. For comparison, the Cu2p core level spectrum of the copper specimen (untreated copper) was also added. The Cu2p profiles in the 925–965 eV binding energy region are quite similar for untreated and blank copper samples, indicating the presence of Cu(I) species (Cu_2O) on the electrode surface in both cases. However, some differences between the two Cu2p core level spectra should be mentioned; namely, in the blank sample, the appearance of satellite signals is observed in the regions 943-948 eV and 962-967 eV that are specific to Cu(II) species, and a small shift in the binding energy to lower values (see Figure 12a). These changes could be due to the existence of a small CuO phase on the copper surface and to the incorporation of chloride into the Cu_2O lattice [72], when the copper electrode was exposed to the test saline solution. These results are consistent with the data obtained from Raman characterization (cf. Figure 8a), where the changes observed for the blank sample were attributed to the formation of chloride-related species on the copper surface.

The Cu2p XPS spectra of samples exposed to solutions containing PyODT demonstrate the significant transformation that occurs on the copper surface (see Figure 12b-c). Thus, in addition to the satellite lines in the 940-945 eV and 960-965 eV regions specific for the Cu(II) species, the Cu2p3/2 and Cu2p1/2 peaks at 934.5 and 954.4 eV [73] can also be observed in Figure 12b-c. The increase in the concentration of PyODT leads to an increase of Cu(II) species on the copper surface and to values of the Cu(I) peaks similar to those obtained for untreated copper. This could be an indication of continuous coverage of the copper surface with the inhibitor film and

less Cl⁻ ions incorporated into the Cu_2O lattice. These observations are in agreement with the electrochemical results, which showed that the inhibition efficiency of PyODT at a concentration of 1.5 mM exceeds 99%.

As shown in Figure 13a-b, the C1s signals are well fitted with four peaks for the two inhibitor concentrations investigated. Therefore, the film formed on the copper surface in the presence of 1 mM PyODT reveals peak maxima with binding energies of ca. 284.4, 285.4, 287.3 and 288.8 eV, respectively. The first three bands have been assigned to carbon species that possess sp^2 hybridization state $C(sp^2)$ for the largest contribution, carbon in C-O/C=N groups, and C-N/C-O-C functions [74], while the remaining one was attributed to carbon in the O-C(N)-S group. A small shift of the peaks alongside the variation of the intensity of the bands (*i.e.* a decrease in the area of the bands assigned to C=N/C-O and C-N/C-O-C groups), and an increase of those assigned to C=C and O-C(N)-S were observed in the XPS spectra of the copper samples after immersion in a solution containing 1.5 mM PyODT (see Figure 13b). These changes highlight that there were small differences in the organization of the PyODT layers on the Cu surface.

Two nitrogenous species can be observed in the XPS N1s spectra of the PyODT film formed on the copper surface (cf. Figure 13c-d). They are located at approximately 398.7 and 399.6 eV and can be attributed to the nitrogen atoms in the pyridyl ring [75] and the oxadiazole groups [32]. These values suggest that the non-protonated N species exist in the composition of the film, regardless the concentration of PyODT. Therefore, it was assumed that the changes observed for the PyODT concentration of 1.5 mM in the case of C1s affected very few nitrogenous sites.

More details on the influence of PyODT concentration on film formation were obtained from the O1s XPS spectra given in Figure 14a,b. Three peaks located at 529.6, 531.1 and 534.7 eV were observed in the XPS spectra of the copper surface after 24 h immersion in a solution containing 1 mM PyODT (cf. Figure 14a). The band at 529.6 eV indicates the presence of Cu-O bonds (O^{2-} from CuO) on the surface of the electrode [76], while the two other signals could be associated with the C-O bonds in the PyODT molecule after its chemisorption on the metal and to adsorbed water [77], respectively. In contrast, a single peak at 531.9 eV, attributed to the C-O bonds in PyODT, could be seen in the XPS spectra of copper immersed in the corrosive solution containing 1.5 mM PyODT. This result suggests complete coverage of the copper surface with an organic inhibitor layer in the solution containing 1.5 mM PyODT concentration.

The spectra recorded for the S2p core level also exhibit different features depending on the concentration of PyODT, as shown in Figure 14c-d. In the presence of 1 mM PyODT, a doublet is observed at approximately 162.5 and 163.7 eV for S2p3/2 and S2p1/2, respectively. These peaks can be associated with chemisorbed sulphur, suggesting a Cu-S interaction between the metal substrate and the layer of the organic inhibitor [78]. On the other hand, when the copper surface was treated with 1.5 mM PyODT, two doublets were detected in the recorded XPS spectrum (see Figure 14d). Among them, the one attributed to the C-S form of the adsorbed PyODT predominates, while the second doublet, located at about 168.1 and 169.3 eV, can be attributed, depending on the position and its relative intensity, to an oxidized sulphur state [78]. The absence of oxidized sulphur species on the copper surface exposed to the solution containing 1 mM PyODT is difficult to explain unless oxidation of PyODT could occur prior to adsorption when a higher concentration of PyODT was involved.

3.3. Scanning microelectrochemical characterization

The heterogeneous degradation of Cu and its inhibition by the presence of PyODT at the concentration of maximum efficiency (i.e., 1.5 mM), was further investigated with the scanning vibrating electrode technique (SVET) in 50 mM NaCl solution. The lower concentration used for these measurements was chosen in order to improve the signal-to-noise ratio of the potential gradients developed by the local ionic concentrations but maintaining a sufficiently aggressive environment for the corrosion reaction to occur. Although this may somewhat compromise the direct intercomparison of the data provided by SVET with those of the conventional electrochemical experiments in Section 3.1, it helps to determine the possible surface heterogeneity of corrosion and protection processes.

Figure 15 shows the current density values detected during scanning of the copper surface in the absence of inhibitor, as well as optical images taken just before the SVET measurements. Dynamically changing positive and negative ionic current densities, reflecting local anodic and cathodic activation, respectively, develop on Cu as a result of corrosion reactions. Dark areas could be observed on the optical images due to the precipitation of corrosion products gradually covering the surface from the edges of the copper where the anodic activity is initially detected. This is evidenced by the appearance of anodic current densities in the upper left corner (cf. Figure 15a),

21

moving towards the upper and middle part of the copper sample (Figure 15c,e), precisely in the same direction as the dark regions advance from optical inspection (Figure 15b,d,f).

Likewise, Figure 16 shows the SVET results obtained with the Cu surface exposed to a 50 mM NaCl solution containing 1.5 mM PyODT during the first hours of immersion. The activity is drastically suppressed in the presence of corrosion inhibitor, the absolute values of the current density being 5 times smaller than in the NaCl solution without inhibitor (note that the same scale is used for the ionic current density in Figures 15 and 16). Furthermore, the optical images did not show significant modification of the metal surface during immersion in the electrolyte for 3-4 h of exposure, unlike the result obtained using Cu under inhibitor-free conditions (cf. the optical images of Figures 15 and 16).

3.4. Quantum chemical calculation

Several publications have shown a relationship between the structure of chemicals, especially organic compounds, and their inhibitory action as effective corrosion inhibitors [79-81]. Computational methods using DFT theory are powerful tools for quantifying the structural features and parameters of the electronic structure of chemical compounds [52,82]. Recently, quantum chemistry has become widely used in the design and development of novel high performance corrosion inhibitors, as well as to analyse the characteristics of the interaction mechanism between the inhibitor and the metal surface mechanism, and to elucidate the structural nature of the inhibitor in the corrosion process [52,81,83]. Heterocyclic oxadiazole-thiol ligands, due to the presence of the thioamide moiety (NHC=S) in their structure, occur in the gaseous phase as thione and thiol tautomers due to prototropic thione-thiol tautomerism reaction involving proton transfers [81,84,85]. In addition, PyODT can be further ionized in aqueous solution according to equation (5). Therefore, theoretical calculations were made considering all forms of the PyODT molecule in the gaseous phase, as well as in solution in the presence of water as the solvent. Figure 17 and Figure 18 show the fully optimized molecular structures of all forms of the inhibitor PyODT and their frontier molecular orbitals (HOMO and LUMO) obtained using the unrestricted B3LYP/6-311^{++}G(d,p) level of theory by applying CPCM model in the presence of water as solvent [49,50].

The selected structural parameters of optimized geometry for all forms of the PyODT molecule in gas phase and in solution are listed in Table 4. Solvation has a significant impact on the bond lengths and bond angles of PyODT species. For the thione form, an increase in the bond

22

length of the C=S group is observed in aqueous solution compared to its counterpart in the gaseous phase (1.6542 vs. 1.6371 Å), which implies a higher reactivity of the C=S group in the aqueous phase. However, the bond length of this group in the thiolate ion of PyODT in solution is greater than the bond length of C=S group in thione, which predicts the higher reactivity of the thiolate ion of PyODT [81]. The selected dihedral angles of each form of the PyODT molecule are shown in Table 4 to be nearly 180º or 0º and reveal that their structures are substantially plane. On the other hand, the pyridyl ring, the oxadiazole ring and the S-H moiety (thiol group) are all in the same plane, which is the plane of the molecule, and considering the frontier molecular orbital theory, such planar geometry contributes to the formation of an integrated and extensive resonance system [81]. This large π-system also allows the back donation of the dπ electron from the Cu metal to the π*-orbital of the inhibitor [86], as well as the strong π-π staking between the inhibitor molecule and the metal surface which increases the chemical adsorption of the inhibitor (see Figure 17a-c and Figure 18j-l). The HOMO density distributions, as shown in Figures 17d-f and Figures 18m-o, are localized primarily in the oxadiazole ring and the S atom, affording nucleophilic interaction of the nonbonding electron pairs available in the N, O and S heteroatoms with the Cu atom on the surface of the metal. The LUMO density distributions shown in Figure 17g-i and Figure 18p-r, are localized mainly on the pyridyl and the oxadiazole rings, which allows the back donation of the dπ electron of the Cu atom to the π*-orbital of these two rings [87,88], thus enhancing their adsorption on the metal surface.

To study the effect of the electronic properties on the inhibition efficiency of the studied compound, key parameters such as E (energy of the molecule), E_{HOMO}, E_{LUMO}, ΔE_{L-H} (LUMO-HOMO gap), and μ (dipole moment), which directly influence the electronic interaction between the inhibitor molecule and the metal surface, were calculated in the gaseous phase and in solution, with the presence of water as solvent, using the DTF theory and the results are listed in Table 5. The values of the HOMO and LUMO energies and ΔE_{L-H} can be correlated with the inhibition efficiency. Thus, a higher E_{HOMO} value and lower values of E_{LUMO} and ΔE_{L-H} lead to a stronger chemisorption of the inhibitor molecule on the metal surface, and as a result, a higher inhibition efficiency is expected [81,84]. The values of these parameters for all forms of the inhibitor in gas phase, as well as in solution (see Table 5), are comparable to the values reported for inhibitors of similar structures [81,82,84,89], which anticipated the high effective corrosion behaviour of this inhibitor.

The electron transfer fraction (ΔN) is an important parameter to determine the chemical potential of the inhibitor-metal interaction [52,81,84]. The number of transferred electrons (ΔN) for PyODT inhibitor and bulk Cu metal surface was calculated for the different forms of the inhibitor both in the gas phase and in solution by the following equation:

$$\Delta N = \frac{(\chi_{Cu} - \chi_{inh})}{2(\eta_{Cu} - \eta_{inh})}$$

(6)

where χ_{Cu} and χ_{inh} are the absolute electronegativity of copper and the inhibitor, and η_{Cu} and η_{inh} are the absolute hardness of copper and the inhibitor, respectively. The theoretical χ value of 14.01 eV mol^{-1} and the η value of 6.28 eV mol^{-1} for Cu were taken from the literature [90-92]. The values of χ_{inh} and η_{inh} are related to the electron affinity (A) and the ionization potential (I) as presented in equations (7) and (8):

$$\chi = \frac{I + A}{2}$$

(7)

$$\eta = \frac{I - A}{2}$$

(8)

where, according to Koopan's theorem, I and A are related to the frontier orbital energies according to equations (9) and (10) [52,81,84]:

$$I = -E_{HOMO}$$

(9)

$$A = -E_{LUMO}$$

(10)

The values of χ_{inh} and η_{inh} for all forms of the inhibitor were calculated using the I and A values obtained from quantum chemical calculations in both gas phase and in solution. According to Lukovits [93], if $\Delta N < 3.6$, the tendencies for chemisorption and the inhibition efficiency increase with increasing electron-donating ability at the metal surface. The calculated ΔN values for the different forms of the PyODT inhibitor (namely, 0.53-0.55; see Table 5) are in agreement with the chemisorption of the inhibitor on the metal surface and predict its effective anticorrosive properties for copper.

The molecular polarity of an organic inhibitor is anticipated by measuring its dipole moment, which is closely correlated with van der Waals interactions [81]. The results in Table 5 show that the solvation has a significant impact on the dipole moments of both the thione and thiol tautomers, as well as on the thiolate ion of PyODT. The dipole moments of the three forms of

PyODT in solution are significantly higher than their counterparts in the gas phase (*e.g.*, thione and thiol values are 4.0308 *vs*. 2.6629 and 3.7211 *vs*. 2.5831 D, respectively). The increased dipole moment can evidence a stronger van der Waals interaction of the inhibitor with the metallic surface in aqueous solution. The dipole moment of the ionic species is especially much higher compared to thione and thiol tautomers, indicating a more favourable configuration for its adsorption on the surface of copper [81]. In addition, the possible existence of the thiolate ion increases the negative charge on the S atom, suggesting physisorption of the inhibitor from this centre on the metal surface, as well as chemisorption. All these features make the studied molecule a powerful corrosion inhibitor and confirm the experimental findings.

In addition, in order to explore the potential metal complexing ability of the inhibitor in solution, it is of great interest to establish how the interaction of the solvent can modify its electronic properties and, therefore, the capacity of the thiol moiety to adsorb on the surface of copper and chelate the Cu ions diffusing into the solution as result of the corrosion process [49]. For this reason, the thione-thiol tautomerism was computed individually in the gas phase and the solution phase under DFT/B3LYP/6-311 G(d,p) level of theory. The QST2 method is used to study the reaction path of the single hydrogen intra-migration between the two optimized tautomers and the structures of the transition states were obtained [51,85]. The energy profiles of thione-thiol tautomerism in the gas and solution phases are shown in Figure 19. The structure of the transition state (TS) of the transferred proton lies between the N and S atoms constructing a four-membered pseudo-heterocyclic ring with N1…H1 and S1…H1 distances of 1.35 and 1.76 Å in the gas phase, respectively, while the N1…H1 distance was increased to 1.36 Å and the S1….H1 distance decreased to 1.75 Å in solution. This result reveals the effect of solvation on the TS structure and shows that, however, the TS structure in the gas phase is comparable to the structure of the thione tautomer, while in solution it seems closer to the structure of the thiol tautomer. The energy differences between the two tautomers and the TS were calculated as the tautomerization energy (ΔE) considering the thione isomer as the zero-point reference energy [51]. The calculated energies of the TS are 22.89 kcal mol^{-1} in the gas phase and 19.77 in solution, which shows that the TS is more stable in solution when water is used as a solvent. The energy difference between thione and thiol tautomers in gas phase is +4.22 kcal mol^{-1}, while this difference is -4.94 kcal mol^{-1} in solution. These results confirm that the thiol isomer is moderately more stable in solution than the thione isomer.

However, as the total energy values of the thiol and thione forms are very close to each other while the activation energy is very low, one cannot conclude from the energy values which tautomer will predominantly exist in the solution phase. Therefore, further studies were carried out to determine the pK_a of both forms of the PyODT inhibitor as an LH ligand because the acidity of the thiol and thione moieties in aqueous solution, due to their R-NH or R-SH functional groups, is an important indicator of their reactivity [94]. The theoretical method based on the DFT calculation for the prediction of pK_a was performed using equation (11) and the thermodynamic cycle given in Figure 20 [95].

$$LH + H_2O \rightarrow L^- + H_3O^+ \tag{11}$$

All calculations were performed using an unrestricted B3LYP/6-311++G(d,p) level of theory by applying the CPCM model in the presence of water as solvent, and the extracted data are listed in Table 6. As shown in Table 6, the corresponding pK_a values for thione and thiol tautomers are 3.77 and -2.62, respectively. This result reveals that the thiol isomer of PyODT is acidic, and by losing its proton, it exists primarily as R-S$^-$ in aqueous solution and causes moderate changes in the thione-thiol tautomeric equilibrium towards the predominance of thiol tautomer. These results are in good agreement with the experimental results of lowering the pH of the solution in the initial time after addition of the inhibitor.

3.5. MD simulation

The MD simulation approach was used to obtain more information on the adsorption behaviour of PyODT on the surface of copper. The equilibrium configuration of PyODT on a Cu (111) surface is shown in Figure 21. It is evident that during the MD simulation process, the PyODT molecule gradually approached the copper surface with almost flat orientation. This parallel adsorption supports the maximum contact and also the highest surface coverage. To obtain more information on the interaction of PyODT on copper surfaces, the values of adsorption energy ($E_{adsorption}$) and the binding energy ($E_{binding}$) between the inhibitory species and the metal surface have been calculated using the following equations [52,96]:

$$E_{adsorption} = E_{total} - \left(E_{surface+solution} + E_{surface+solution} \right) + E_{solution} \tag{12}$$

$$E_{binding} = -E_{adsorption} \tag{13}$$

where E_{total} represents the total energy of the simulation system and comprises the copper crystal together with the inhibitor molecule adsorbed on the copper surface and the solution; $E_{surface+solution}$ is the potential energy of the system without the inhibitor; $E_{inhibitor+solution}$ is the potential energy of the system without the metal surface; and $E_{solution}$ is the potential energy of the aqueous solution. The values of the interaction energies for the system were evaluated and are summarized in Table 7. The negative sign of $E_{adsorption}$ implies that the interaction between the PyODT species and the copper surface is spontaneous, strong, and stable.

4. Conclusions

The efficiency of 5-(4-pyridyl)-1,3,4-oxadiazole-2-thiol as a novel inhibitor against corrosion of copper has been demonstrated in 3.5 wt.% NaCl solution, and a mechanism of adsorption leading to the development of protective films has been proposed. The predictions of large corrosion protection effects expected when examining the molecular structure and functional groups present were confirmed by multiscale electrochemical characterization and simulation of the interaction mechanisms between the inhibitor and the copper surface. Electrochemical studies revealed high inhibition efficiency of PyODT at concentrations of 1 and 1.5 mM, supporting the gradual development of a protective inhibitory film on the metallic surface. Inhibition efficiencies greater than 99% and a markedly improved and compact protective film were obtained on the copper surface at about 24 h of immersion in a corrosive medium containing PyODT. SVET analysis showed that the suppression of heterogeneous corrosion activity was significant even in the first hours of exposure to the solution containing 1.5 mM PyODT. The resulting protective film appears compact on SEM inspection, and composed primarily of the organic molecules, as supported by EDX and XPS data, revealing the presence of the heteroatoms and the functional groups of PyODT.

XPS data obtained after exposure to 3.5 wt.% NaCl + 1.5 mM PyODT reveals that copper oxide is barely present on the surface, when the compact inhibitory film was formed, but interactions of Cu-O with the organic molecules are dominant.

Quantum chemistry calculations in the gas phase and in solution with water as a solvent, combined with Molecular Dynamics studies, suggest that the main interaction between the metal and PyODT occurs through the thiol and oxadiazole groups. The deprotonated nitrogenous structures of the tautomeric equilibrium seem to be favoured according to Raman and XPS

27

analysis. Then the trend towards a planar configuration of the molecule is established, thus favouring the interaction of the inhibitory molecule with the surface of copper.

A Machine Learning approach applied to Raman spectra collected from the copper surface exposed for different time periods to blank and PyODT-containing corrosive solutions allowed adequate discrimination between corroded and inhibitor-protected samples. The obtained results first highlight the potential of Raman spectroscopy in conjunction with Machine Learning algorithms for its application in corrosion inhibition studies. This approach offers a promising alternative to follow the evolution over time of the films formed on metallic surfaces under various experimental conditions and, at the same time, can successfully contribute to the identification of corrosion sites by a rapid, inexpensive and non-destructive method such as Raman spectroscopy.

Acknowledgments

References

[1] E.S.M. Sherif, A.M. El Shamy, M.M. Ramla, A.O.H. El Nazhawy, 5-(Phenyl)-4H-1,2,4-triazole-3-thiol as a corrosion inhibitor for copper in 3.5% NaCl solutions, Mater. Chem. Phys. 102 (2007) 231-239. https://doi.org/10.1016/j.matchemphys.2006.12.009.

[2] H. Tian, Y.F. Cheng, W. Li, B. Hou, Triazolyl-acylhydrazone derivatives as novel inhibitors for copper corrosion in chloride solutions, Corros. Sci. 100 (2015) 341-352. https://doi.org/10.1016/j.corsci.2015.08.022.

[3] Y. Qiang, S. Zhang, L. Guo, X. Zhen, B. Xiang, S. Chen, Experimental and theoretical studies of four allyl imidazolium-basedionic liquids as green inhibitors for copper corrosion in sulfuric acid, Corros. Sci. 119 (2017) 68-78. https://doi.org/10.1016/j.corsci.2017.02.021.

[4] H. Huang, Z. Wang, Y. Gong, F. Gao, Z. Luo, S. Zhang, H. Li, Water soluble corrosion inhibitors for copper in 3.5 wt% sodium chloride solution, Corros. Sci. 123 (2017) 339-350. https://doi.org/10.1016/j.corsci.2017.05.009.

[5]   M.M. Antonijevic, M.B. Petrovic, Copper corrosion inhibitors. A review, Int. J. Electrochem. Sci. 3 (2008) 1-28.

[6]   N. Kovacević, H.O. Curkovic, E. Stupnisek-Lisac, H. Takenouti, The influence of pH value on the efficiency of imidazole based corrosion inhibitors of copper, Corros. Sci. 52 (2010) 398-405. https://doi.org/10.1016/j.corsci.2009.09.026.

[7]   M. Finšgar, I. Milošev, Inhibition of copper corrosion by 1,2,3-benzotriazole: A review, Corros. Sci. 52 (2010) 2737-2749. https://doi.org/10.1016/j.corsci.2010.05.002.

[8]   F.M. Al Kharafi, I.M. Ghayad, R.M. Abdallah, Corrosion inhibition of copper in seawater by 4-amino-4H-1,2,4-triazole-3-thiol, Corrosion 69 (2013) 58-66. https://doi.org/10.5006/0556.

[9]   M.B. Petrović Mihajlović, M.B. Radovanović, Ž.Z. Tasić, M.M. Antonijević, Imidazole based compounds as copper corrosion inhibitors in seawater, J. Mol. Liq. 225 (2017) 127-136. https://doi.org/10.1016/j.molliq.2016.11.038.

[10] I.A. Arkhipushkin, M.O. Agafonkina, L.P. Kazansky, Y.I. Kuznetsov, K.S. Shikhaliev, Characterization of adsorption of 5-carboxy-3-amino-1,2,4-triazole towards copper corrosion prevention in neutral media, Electrochim. Acta 308 (2019) 392-399. https://doi.org/10.1016/j.electacta.2019.04.014.

[11] A. Mishra, J. Aslamb, C. Vermac, M.A. Quraishi, E.E. Ebenso, Imidazoles as highly effective heterocyclic corrosion inhibitors for metals and alloys in aqueous electrolytes: A review, J. Taiwan. Inst. Chem. E. 114 (2020) 341-358. https://doi.org/10.1016/j.jtice.2020.08.034.

[12] H. Huang, X. Guo, The relationship between the inhibition performances of three benzo derivatives and their structures on the corrosion of copper in 3.5 wt.% NaCl solution, Colloid. Surface. A. 598 (2020) 124809. https://doi.org/10.1016/j.colsurfa.2020.124809.

[13] E. Stupnišek-Lisac, A. Brnada, A.D. Mance, Secondary amines as copper corrosion inhibitors in acid media, Corros. Sci. 42 (2000) 243-257. https://doi.org/10.1016/S0010-938X(99)00065-7.

[14] E.M. Sherif, S.M. Park, Inhibition of copper corrosion in acidic pickling solutions by N-phenyl-1,4-phenylenediamine, Electrochim. Acta 51 (2006) 4665-4673. https://doi:10.1016/j.electacta.2006.01.007.

[15] R. Farahati, H. Behzadi, S. Morteza Mousavi-Khoshdel, A. Ghaffarinejad, Evaluation of corrosion inhibition of 4-(pyridin-3-yl) thiazol-2-amine for copper in HCl by experimental and theoretical studies, J. Mol. Struct. 1205 (2020) 127658. https://doi.org/10.1016/j.molstruc.2019.127658.

[16] S.L. Li, Y.G. Wang, S.H. Chen, R. Yu, S.B. Lei, H.Y Ma, De X Liu, Some aspects of quantum chemical calculations for the study of Schiff base corrosion inhibitors on copper in NaCl solutions, Corros. Sci. 41 (1999) 1769-1782. https://doi.org/10.1016/S0010-938X(99)00014-1.

[17] Y. Zhou, S. Zhang, L. Guo, S. Xu, H. Lu, F. Gao, Studies on the effect of a newly synthesized Schiff base compound on the corrosion of copper in 3% NaCl solution, Int. J. Electrochem. Sc. 10 (2015) 2072-2087.

[18] D. S. Chauhan P. Singh, M.A. Quraishi, Quinoxaline derivatives as efficient corrosion inhibitors: Current status, challenges and future perspectives, J. Mol. Liq. 320 (2020), 114387. https://doi.org/10.1016/j.molliq.2020.114387.

[19] C. Verma, M.A. Quraishi, E.E. Ebenso, Quinoline and its derivatives as corrosion inhibitors: A review, Surf. Interfaces 21 (2020) 100634. https://doi.org/10.1016/j.surfin.2020.100634.

[20] K.M. Ismail, Evaluation of cysteine as environmentally friendly corrosion inhibitor for copper in neutral and acidic chloride solutions, Electrochim. Acta 52 (2007) 7811-7819. https://doi.org/10.1016/j.electacta.2007.02.053.

[21] D.Q. Zhang, Q.R. Cai, L.X. Gao, K.Y. Lee, Effect of serine threonine and glutamic acid on the corrosion of copper in aerated hydrochloric acid solution, Corros. Sci. 50 (2008) 3615-3621. https://doi.org/10.1016/j.corsci.2008.09.007.

[22] D.Q. Zhang, Q.R. Cai, X.M. He, L.X. Gao, G.D. Zhou, Inhibition effect of some amino acids on copper corrosion in HCl solution, Mater. Chem. Phys. 112 (2008) 353-358. https://doi.org/10.1016/j.matchemphys.2008.05.060.

[23] F. Bentiss, M. Traisnel, M. Lagrenee, The substituted 1,3,4-oxadiazoles: a new class of corrosion inhibitors of mild steel in acidic media, Corros. Sci. 42 (2000) 127-146. https://doi.org/10.1016/S0010-938X(99)00049-9.

[24] F. Bentiss, M. Traisnel, H. Vezin, H.F. Hildebrand, M. Lagrenee, 2,5-Bis(4-dimethylaminophenyl)-1,3,4-oxadiazole and 2,5-bis(4-dimethylaminophenyl)-1,3,4-

thiadiazole as corrosion inhibitors for mild steel in acidic media, Corros. Sci. 46 (2004) 2781-2792. https://doi.org/10.1016/j.corsci.2004.04.001.

[25] S. Bala, S. Kamboj, A. Kajal, V. Saini, D.N. Prasad, 2014. 1,3,4-Oxadiazole derivatives: Synthesis, characterization, antimicrobial potential, and computational studies, Biomed Res. Int., 172791. https://doi.org/10.1155/2014/172791.

[26] M. Aruna Sindhe, Y.D. Bodke, R. Kenchappa, S. Telkar, A. Chandrashekar, Synthesis of a series of novel 2,5-disubstituted-1,3,4-oxadiazole derivatives as potential antioxidant and antibacterial agents, J. Chem. Biol. 9 (2016) 79-90. https://doi.org/10.1007/s12154-016-0153-9.

[27] R. Palit, N. Saraswat, J. Sahoo, Review on substituted 1,3,4-oxadiazole and its biological activities, Int. Res. J. Pharm. 7(2) (2016) 1-7. https://doi.org/10.7897/2230-8407.07212.

[28] M. Lebrini, F. Bentiss, H. Vezin, M. Lagrenee, Inhibiting effects of some oxadiazole derivatives on the corrosion of mild steel in perchloric acid solution, Appl. Surf. Sci. 252 (2005) 950-958. https://doi.org/10.1016/j.apsusc.2005.01.160.

[29] M. Bouklah, B. Hammouti, M. Lagrenee, F. Bentiss, Thermodynamic properties of 2,5-bis(4-methoxyphenyl)-1,3,4-oxadiazole as a corrosion inhibitor for mild steel in normal sulfuric acid medium, Corros. Sci. 48 (2006) 2831-2842. https://doi.org/10.1016/j.corsci.2005.08.019.

[30] G.M. Doddahosuru, K.N. Mohana, Synthesis of new pyridine based 1,3,4-oxadiazole derivatives and their corrosion inhibition performance on mild steel in 0.5 M hydrochloric acid, Ind. Eng. Chem. Res. 53 (2014) 2092-2105, https://doi.org/10.1021/ie402042d.

[31] A. Rochdi, R. Touir, M. El Bakri, M. E. Touhami, S. Bakkali, B. Mernari, Protection of low carbon steel by oxadiazole derivatives and biocide against corrosion in simulated cooling water system, J. Eviron. Chem. Eng. 3 (2015) 233-242. https://doi.org/10.1016/j.jece.2014.11.020.

[32] M. Bouanis, M. Tourabi, A. Nyassi, A. Zarrouk, C. Jama, F. Bentiss, Corrosion inhibition performance of 2,5-bis(4-dimethylaminophenyl)-1,3,4-oxadiazole for carbon steel in HCl solution: Gravimetric, electrochemical and XPS studies, Appl. Surf. Sci. 389 (2016) 952-966. https://doi.org/10.1016/j.apsusc.2016.07.115.

[33] P.R. Ammal, M. Prajila, A. Joseph, Effective inhibition of mild steel corrosion in hydrochloric acid using EBIMOT, a 1,3,4-oxadiazole derivative bearing a 2-

ethylbenzimidazole moiety: Electro analytical, computational and kinetic studies, Egypt. J. Pet. 27 (2018) 823-833. https://doi.org/10.1016/j.ejpe.2017.12.004.

[34] P.R. Ammal, M. Prajila, A. Joseph, Effect of substitution and temperature on the corrosion inhibition properties of benzimidazole bearing 1, 3, 4-oxadiazoles for mild steel in sulphuric acid: Physicochemical and theoretical studies, J. Eviron. Chem. Eng. 6 (2018) 1072-1085. https://doi.org/10.1016/j.jece.2018.01.031.

[35] X.J. Raj, N. Rajendran, Effect of some oxadiazole derivatives on the corrosion inhibition of brass in natural seawater, J. Mater. Eng. Perform. 21 (2012) 1363-1373. https://doi.org/10.1007/s11665-011-0007-0.

[36] K. Chadrasekaran, B.S. Alwar, R. Ravichandran, Inhibition of oxadiazole derivatives for the control of corrosion of copper-nickel alloy in sea water, J. Adv. Electrochem. 2 (2016) 121-125. https://doi.org/10.30799/jaec.

[37] A. Rochdi, O. Kassou, N. Dkhireche, R. Touir, M. El Bakri, M. Ebn Touhami, M. Sfaira, B. Mernari, B. Hammouti, Inhibitive properties of 2,5-bis(n-methylphenyl)-1,3,4-oxadiazole and biocide on corrosion, biocorrosion and scaling controls of brass in simulated cooling water, Corros. Sci. 80 (2014) 442-452. https://doi.org/10.1016/j.corsci.2013.11.067.

[38] S. Gapil, M. Ebadi, W.J. Basirun, A. Hasan, K. Awang, M.A. Golsefidi, M.N. Azmi, M.Y. Sulaiman, Synthesis of heterocyclic compounds of 5-substituted-1,3,4-oxadiazole-2-thiols for the prevention of nickel corrosion, Int. J. Electrochem. Sc. 10 (2015) 1543-1554.

[39] T.F. Paulo, M.A.S. Silva, S.O. Pinheiro, E. Meyer, L.S. Pinheiro, J.A. Freire, A.A. Tanaka, P.L. Neto, I.S. Moreira, I.C.N. Diogenes, 5-(4-Pyridinyl)-1,3,4-oxadiazole-2-thiol on gold: SAM formation and electroactivity, J. Brazil. Chem. Soc. 19 (2008) 711-719. https://doi.org/10.1590/S0103-50532008000400015.

[40] F. Lussier, V. Thibault, B. Charron, G. Q. Wallace, J.-F. Masson, Deep learning and artificial intelligence methods for Raman and surface-enhanced Raman scattering, TrAC Trends in Analytical Chemistry 124 (2020) 115796. https://doi.org/10.1016/j.trac.2019.115796.

[41] I. Olaetxea, A. Valero, E. Lopez, H. Lafuente, A. Izeta, I. Jaunarena, A. Seifert, Machine learning-assisted Raman spectroscopy for pH and lactate sensing in body fluids, Anal. Chem. 92 (2020) 13888–13895. https://doi.org/10.1021/acs.analchem.0c02625.

[42] A.C. Bastos, M.C. Quevedo, O.V. Karavai, M.G.S. Ferreira, Review—On the application of the Scanning Vibrating Electrode Technique (SVET) to corrosion research, J. Electrochem. Soc. 164 (2017) C973-C990. https://doi.org/10.1149/2.0431714jes.

[43] J.R. Quinlan, Induction of decision trees, Mach. Learn. 1 (1986) 81-106. https://doi.org/10.1007/BF00116251.

[44] A.E. Usoro, Multivariable discriminant analysis; Application of a three-dimensional case on students measurements, Am. J. Appl. Math. Stat. 5 (2015) 123-127. https://doi.org/10.5923/j.ajms.20150503.03.

[45] C. Cortes, V. Vapnik, Support-vector networks, Mach. Learn. 20 (1995) 273-297. https://doi.org/10.1007/BF00994018.

[46] K.Q. Weinberger, L.K. Saul, Distance metric learning for large margin nearest neighbour classification, J. Mach. Learn. Res. 10 (2009) 207-244.

[47] T.G. Dietterich, Ensemble methods in Machine Learning, in: J. Kittler, F. Roli (Eds.), Multiple Classifier Systems. MCS 2000. Lecture Notes in Computer Science, Springer, Berlin, Heidelberg, 2000, vol 1857, pp. 1-15. https://doi.org/10.1007/3-540-45014-9_1.

[48] M. Frisch, G. Trucks, H. Schlegel, G. Scuseria, M. Robb, J. Cheeseman, G. Scalmani, V. Barone, B. Mennucci, G. Petersson, Gaussian 09W, revision A. 02, Gaussian Inc, Wallingford, CT, USA, 2009.

[49] E. Ferrari, M. Saladini, F. Pignedoli, F. Spagnolo, R. Benassi, Solvent effect on keto–enol tautomerism in a new b-diketone: A comparison between experimental data and different theoretical approaches, New J. Chem. 35 (2011) 2840–2847. https://doi.org/10.1039/C1NJ20576E.

[50] M. Cossi, N. Rega, G. Scalmani, V. Barone, Energies, structures, and electronic properties of molecules in solution with the C-PCM solvation model, J. Comput. Chem. 24 (2003) 669–681. https://doi.org/10.1002/jcc.10189.

[51] M.R. Aouad, M. Messali, N. Rezki, N. Al-Zaqri, I. Warad, Single proton intramigration in novel 4-phenyl-3-((4-phenyl-1H-1,2,3-triazol-1-yl)methyl)-1H-1,2,4-triazole-5(4H)-thione: XRD-crystal interactions, physicochemical, thermal, Hirshfeld surface, DFT realization of thiol/thione tautomerism, J. Mol. Liq. 264 (2018) 621–630. https://doi.org/10.1016/j.molliq.2018.05.085.

[52] M. Talebian, K. Raeissi, M. Atapour, B.M. Fernández-Pérez, Z. Salarvand, S. Meghdadi, M. Amirnasr, R.M. Souto, Inhibitive effect of sodium (E)-4-(4-nitrobenzylideneamino) benzoate on the corrosion of some metals in sodium chloride solution, Appl. Surf. Sci. 447 (2018) 852-865. https://doi.org/10.1016/j.apsusc.2018.04.073.

[53] H. Sun, COMPASS: An ab initio force-field optimized for condensed-phase applications overview with details on alkane and benzene compounds, J. Phys. Chem. B 102 (1998) 7338-7364. https://doi.org/10.1021/jp980939v.

[54] W. Qafsaoui, M.W. Kendig, S. Joiret, H. Perrot, H. Takenouti, Ammonium pyrrolidine dithiocarbamate adsorption on copper surface in neutral chloride media, Corros. Sci. 106 (2016) 96-107. https://doi.org/10.1016/j.corsci.2016.01.029.

[55] Z. Khiati, A.A. Othman, M. Sanchez-Moreno, M.-C. Bernard, S. Joiret, E.M.M. Sutter, Corrosion inhibition of copper in neutral chloride media by a novel derivative of 1,2,4-triazole, Corros. Sci. 53 (2011) 3092-3099. https://doi.org/10.1016/j.corsci.2011.05.042.

[56] W. Qafsaoui, H. Huang, X. Guo, The relationship between the inhibition performances of three benzo derivatives and their structures on the corrosion of copper in 3.5 wt.% NaCl solution, Colloid. Surf. A Physicochem. Eng. Asp. 598 (2020) 124809. https://doi.org/10.1016/j.colsurfa.2020.124809.

[57] H. Tian, W. Li, K. Cao, B. Hou, Potent inhibition of copper corrosion in neutral chloride media by novel non-toxic thiadiazole derivatives, Corros. Sci. 73 (2013) 281-291. https://doi.org/10.1016/j.corsci.2013.04.017.

[58] J.R. Macdonald, Note on the parameterization of the constant-phase admittance element, Solid. State. Ion. 13 (1984) 147-149. https://doi.org/10.1016/0167-2738(84)90049-3.

[59] C.H. Hsu, F. Mansfeld, Concerning the conversion of the constant phase element parameter Y_0 into a capacitance, Corrosion. 57 (2001) 747-748. https://doi.org/10.5006/1.3280607.

[60] J.B. Jorcin, M.E. Orazem, N. Pébère, B. Tribollet, CPE analysis by local electrochemical impedance spectroscopy, Electrochim. Acta 51 (2006) 1473-1479. https://doi.org/10.1016/j.electacta.2005.02.128.

[61] G.J. Brug, A.L.G. van den Eeden, M. Sluyters-Rehbach, J.H. Sluyters, The analysis of electrode impedances complicated by the presence of a constant phase element, J. Electroanal. Chem. 176 (1984) 275. https://doi.org/10.1016/S0022-0728(84).

[62] H. Otmacic Curkovic, E. Stupnisek-Lisac, H. Takenouti, Electrochemical quartz crystal microbalance and electrochemical impedance spectroscopy study of copper corrosion inhibition by imidazoles, Corros. Sci. 51 (2009) 2342-2348. https://doi.org/10.1016/j.corsci.2009.06.018.

[63] W. Qafsaoui, A. Et Taouil, M.W. Kendig, H. Cachet, S. Joiret, H. Perrot, H. Takenouti, Coupling of electrochemical, electrogravimetric and surface analysis techniques to study dithiocarbamate/bronze interactions in chloride media, Corros. Sci. 130 (2018) 190-202. https://doi.org/10.1016/j.corsci.2017.10.034.

[64] G. Kear, B.D. Barker, F.C. Walsh, Electrochemical corrosion of unalloyed copper in chloride media-a critical review, Corros. Sci. 46 (2004) 109-135. https://doi.org/10.1016/S0010-938X(02)00257-3.

[65] I. Milošev, N. Kovačević, J. Kovač, A. Kokalj, The roles of mercapto, benzene and methyl groups in the corrosion inhibition of imidazoles on copper: I. Experimental characterization, Corros. Sci. 98 (2015) 107-118. https://doi.org/10.1016/j.corsci.2015.05.006.

[66] M. Rashad, M. Rusing, G. Berth, K. Lischka, A. Pawlis, CuO and Co_3O_4 nanoparticles: Synthesis, characterizations, and Raman spectroscopy, J. Nanomater. (2013) 714853. https://doi.org/10.1155/2013/714853.

[67] W. Qafsaoui, M.W. Kendig, S. Joiret, H. Perrot, H. Takenouti, Ammonium pyrrolidine dithiocarbamate adsorption on copper surface in neutral chloride media, Corros. Sci. 106 (2016) 96-107. https://doi.org/10.1016/j.corsci.2016.01.029.

[68] M. Hamdi, A. Oueslati, I. Chaabane, F. Hlel, 2012. Characterization and electrical properties of $[C_6H_9N_2]_2CuCl_4$ compound, ISRN Condens. Matter. Phys. 750497. https://doi.org/10.5402/2012/750497.

[69] T.F. Paulo, R.A. Ando, I.C.N. Diogenes, M.L.A. Temperini, Understanding the equilibria of thio compounds adsorbed on gold by surface-enhanced Raman Scattering and Density Functional Theory Calculations, J. Phys. Chem. C 117 (2013) 6275-6283. https://doi.org/10.1021/jp400235y.

[70] M. Du, X.J. Zhao, J.H. Guo, 5-(4-Pyridyl)-1,3,4-oxadiazole-2(3H)-thione, Acta Cryst. E60 (2004) o327-o328. https://doi.org/10.1107/S1600536804001916.

[71] R. Sun, J. Yao, S. Li, R. Gu, Raman spectroscopic and density functional theory studies on a benzothiazole-2-thione derivative, Vibrational Spectroscopy 47 (2008) 38-43. https://doi.org/10.1016/j.vibspec.2008.01.018.

[72] W. Ci, W.C. Tu, W.Y. Uen, S.M. Lan, J.X. Zeng, T.N. Yang, C.C. Shen, J.C. Jhao, Chlorine-doped n-type cuprous oxide films fabricated by chemical bath deposition, J. Electrochem. Soc. 161 (2014) D321-D326. http://dx.doi.org/10.1149/2.013406jes.

[73] XPS Interpretation of Copper. https://xpssimplified.com/elements/copper.php, 2020 (accessed 18 October 2020).

[74] G. Zhang, P. Wang, W.-T. Lu, C.-Y. Wang, Y.-K. Li, C. Ding, J. Gu, X.-S. Zheng, F.-F. Cao, Co nanoparticles/Co, N, S tri-doped graphene templated from in-situ formed Co, S Co-doped g-C3N4 as an active bifunctional electrocatalyst for overall water splitting, ACS Appl. Mater. Interf. 9 (2017) 28566-28576. https://doi.org/10.1021/acsami.7b08138.

[75] R.J.J. Jansen, H. van Bekkum, XPS of nitrogen-containing functional groups on activated carbon, Carbon 33 (1995) 1021-1027. https://doi.org/10.1016/0008-6223(95)00030-H.

[76] J. Yuan, J.-J. Zhang, M.-P. Yang, W.-J. Meng, H. Wang, J.-X. Lu, CuO nanoparticles supported on TiO$_2$ with High efficiency for CO$_2$ electrochemical reduction to ethanol, Catalysts 8 (2018) 171. https://doi.org/10.3390/catal8040171.

[77] Y. Lei, G. Gao, W. Liu, T. Liu, Y. Yin, Synthesis of silver nanoparticles on surface-functionalized multi-walled carbon nanotubes by ultraviolet initiated photo-reduction method, Appl. Surf. Sci. 317 (2014) 49–55. https://doi.org/10.1016/j.apsusc.2014.08.054.

[78] F. Bensebaa, Y. Zhou, Y. Deslandes, E. Kruus, T.H. Ellis, XPS study of metal-sulfur bonds in metal-alkanethiolate materials, Surf. Sci. 405 (1998) L472-L476. https://doi.org/10.1016/S0039-6028(98)00097-1.

[79] F. Bentiss, M. Lagrenée, M. Traisnel, 2,5-Bis(n-pyridyl)-1,3,4-oxadiazoles as corrosion inhibitors for mild steel in acidic media, Corrosion 56 (2000) 733-742. https://doi.org/10.5006/1.3280577.

[80] M. Outirite, M. Lagrenée, M. Lebrini, M. Traisnel, C. Jama, H. Vezin, F. Bentiss, AC impedance, X-ray photoelectron spectroscopy and density functional theory studies of 3,5-bis(n-pyridyl)-1,2,4-oxadiazoles as efficient corrosion inhibitors for carbon steel surface in hydrochloric acid solution, Electrochim. Acta. 55 (2010) 1670-1681. https://doi.org/10.1016/j.electacta.2009.10.048.

[81] X. Yang, Y. Huang, G. Liu, J. Liu, L. Ma, X. Niu, X. Qu, A DFT prediction on the chemical reactivity of novel azolethione derivatives as chelating agents: Implications for copper minerals flotation and copper corrosion inhibition, J. Taiwan. Inst. Chem. Eng. 93 (2018) 109-123. https://doi.org/10.1016/j.jtice.2018.09.022.

[82] A.N. Dina, Inhibition efficiency and corrosion rate studies of mild steel in nitric acid using 2-thioacetic acid-5-pyridyl-1,3,4-oxadiazole complexes, Int. J. Corros. Scale Inhib. 8 (2019) 717-725. http://dx.doi.org/10.17675/2305-6894-2019-8-3-18.

[83] F. Bentiss, B. Mernari, M. Traisnel, H. Vezin, M. Lagrenée, On the relationship between corrosion inhibiting effect and molecular structure of 2,5-bis (n-pyridyl)-1,3,4-thiadiazole derivatives in acidic media: AC impedance and DFT studies, Corros. Sci. 53 (2011) 487-495. https://doi.org/10.1016/j.corsci.2010.09.063.

[84] P.R. Ammal, A. Prasad, S. John, A. Joseph, Protection of mild steel in hydrochloric acid using methyl benzimidazole substituted 1,3,4-oxadiazole: Computational, electroanalytical, thermodynamic and kinetic studies, J. Adhes. Sci. Technol. 33 (2019) 2227-2249. https://doi.org/10.1080/01694243.2019.1637169.

[85] M.R. Aouad, M. Messali, N. Rezki, M.A. Said, D. Lentz, L. Zubaydi, I. Warad, Hydrophobic pocket docking, double-proton prototropic tautomerism in contradiction to single-proton transfer in thione ⇔thiol Schiff base with triazole-thione moiety: Green synthesis, XRD and DFT-analysis, J. Mol. Liq. 1180 (2019) 455-461. https://doi.org/10.1016/j.molstruc.2018.12.010.

[86] J. Zhou, S. Chen, L. Zhang, Y. Feng, H. Zhai, Studies of protection of self-assembled films by 2-mercapto-5-methyl-1,3,4-thiadiazole on iron surface in 0.1 M H_2SO_4 solutions, J. Electroanal. Chem. 612 (2008) 257-268. https://doi.org/10.1016/j.jelechem.2007.10.011.

[87] M. Morad, A.K. El-Dean, 2, 2′-Dithiobis(3-cyano-4,6-dimethylpyridine): A new class of acid corrosion inhibitors for mild steel, Corros. Sci. 48 (2006) 3398-3412. https://doi.org/10.1016/j.corsci.2005.12.006

[88] M. Behpour, S.M. Ghoreishi, N. Mohammadi, M., Salavati-Niasari, Investigation of the inhibiting effect of N-[(Z)-1-phenylemethyleidene]-N-{2-[(2-{[(Z)-1phenylmethylidene]amino}phenyl)disulfanyl]phenyl} amine and its derivatives on the corrosion of stainless steel 304 in acid media, Corros. Sci. 53 (2011) 3380-3387. https://doi.org/10.1016/j.corsci.2011.06.017.

[89] F. Bentiss, M. Traisnel, H. Vezin, M. Lagrenée, Linear resistance model of the inhibition mechanism of steel in HCl by triazole and oxadiazole derivatives: Structure–activity correlations, Corros. Sci. 45 (2003) 371-380. https://doi.org/10.1016/S0010-938X(02)00102-6.

[90] R.G. Pearson, Absolute electronegativity and hardness: Application to inorganic chemistry, Inorg. Chem. 27 (1988) 734-740. https://doi.org/10.1021/ic00277a030.

[91] R.M. Issa, M.K. Awad, F.M. Atlam, Quantum chemical studies on the inhibition of corrosion of copper surface by substituted uracils, Appl. Surf. Sci. 255 (2008) 2433-2441. https://doi.org/10.1016/j.apsusc.2008.07.155.

[92] K. Khaled, A.M. Amin, N. Al-Mobarak, On the corrosion inhibition and adsorption behaviour of some benzotriazole derivatives during copper corrosion in nitric acid solutions: A combined experimental and theoretical study, J. Appl. Electrochem. 40 (2010) 601-613. https://doi.org/10.1007/s10800-009-0035-8.

[93] I. Lukovits, E. Kalman, F. Zucchi, Corrosion inhibitors-Correlation between electronic structure and efficiency, Corrosion 57 (2001) 3-8. https://doi.org/10.5006/1.3290328.

[94] Y. Zheng, W. Zheng, D. Zhu, H. Chang, Theoretical modeling of pKa's of thiol compounds in aqueous solution, New J. Chem. 43 (2019) 5239-5254. https://doi.org/10.1039/C8NJ06259E.

[95] J.R. Pliego Jr., Thermodynamic cycles and the calculation of pKa, Chem. Phys. Lett. 367 (2003) 145-149. https://doi.org/10.1016/S0009-2614(02)01686-X.

[96] H. Heydari, M. Talebian, Z. Salarvand, K. Raeissi, M. Bagheri, M.A. Golozar, Comparison of two Schiff bases containing O-methyl and nitro substitutes for corrosion inhibiting of mild steel in 1 M HCl solution, J. Mol. Liq. 254 (2018) 177-187. https://doi.org/10.1016/j.molliq.2018.01.112.
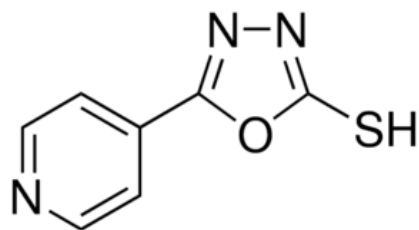
Figure 1. Molecular structure of 5-(4-pyridyl)-1,3,4-oxadiazole-2-thiol (PyODT).
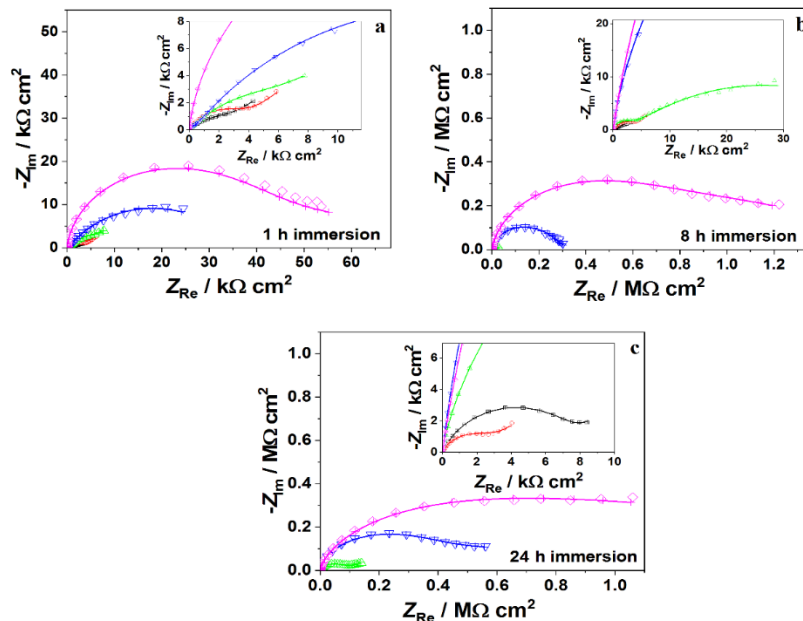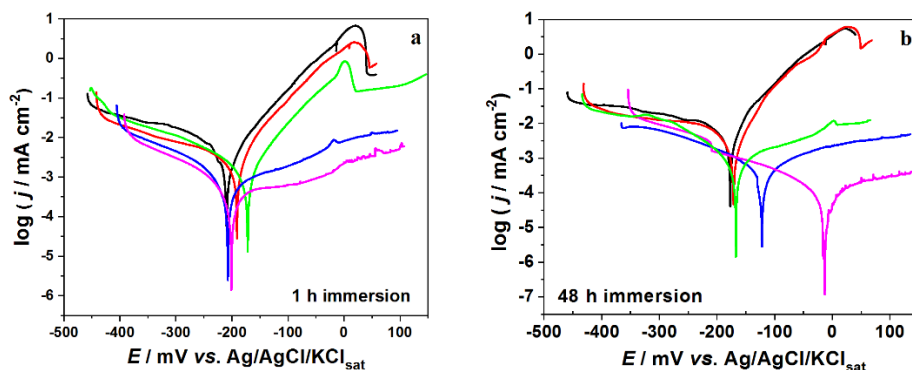
Figure 2. Nyquist diagrams of copper samples in 3.5 wt.% NaCl solution in the absence (□) and in the presence of PyODT at concentrations: (○) 0.25, (△) 0.5, (▽) 1, and (◇) 1.5 mM. The spectra were recorded at different immersion times in the test solution as indicated. Inserts present the Nyquist diagrams in an enlarged scale. The symbols correspond to the measured data and the solid lines with crosses (—+—) to the simulated results using the equivalent circuits given in Figure 4.
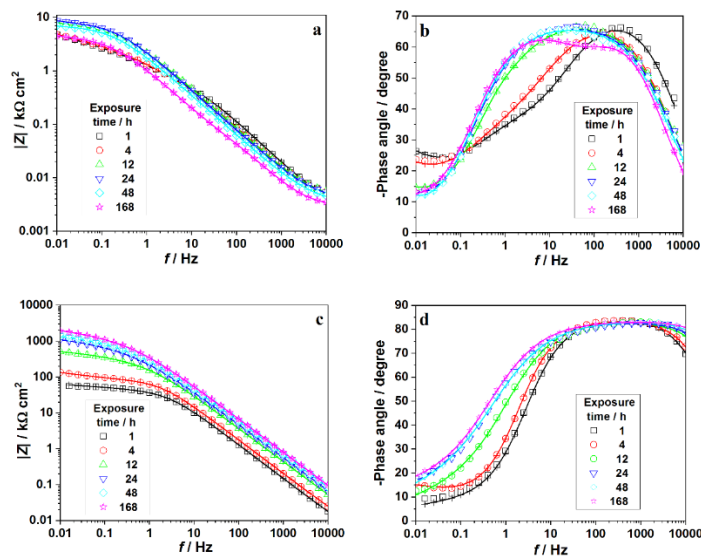

Figure 3. Bode plots of copper samples in 3.5 wt.% NaCl solution in the absence (a, b) and in the presence of 1.5 mM PyODT (c, d). The spectra were recorded at different immersion times in the test solution as indicated. The symbols correspond to the measured data and the solid lines with crosses (—+—) to the simulated results using the equivalent circuits given in Figure 4.
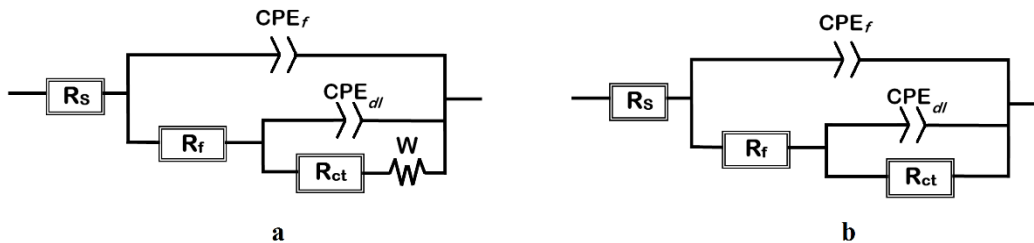
Figure 4. Equivalent circuit models used to fit the EIS experimental data.
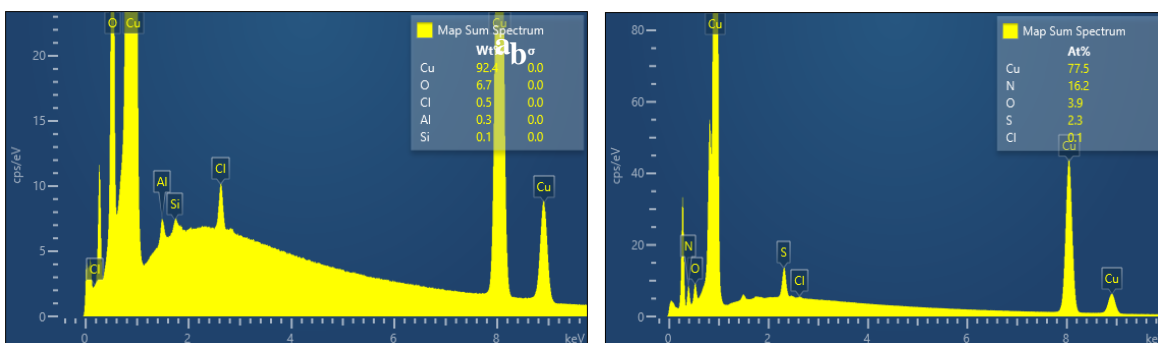

Figure 5. Potentiodynamic polarization curves recorded for copper samples immersed in 3.5 wt.% NaCl solution in the absence (—) and in the presence of different PyODT concentrations: (—) 0.25; (—) 0.5; (—) 1, and (—) 1.5 mM.
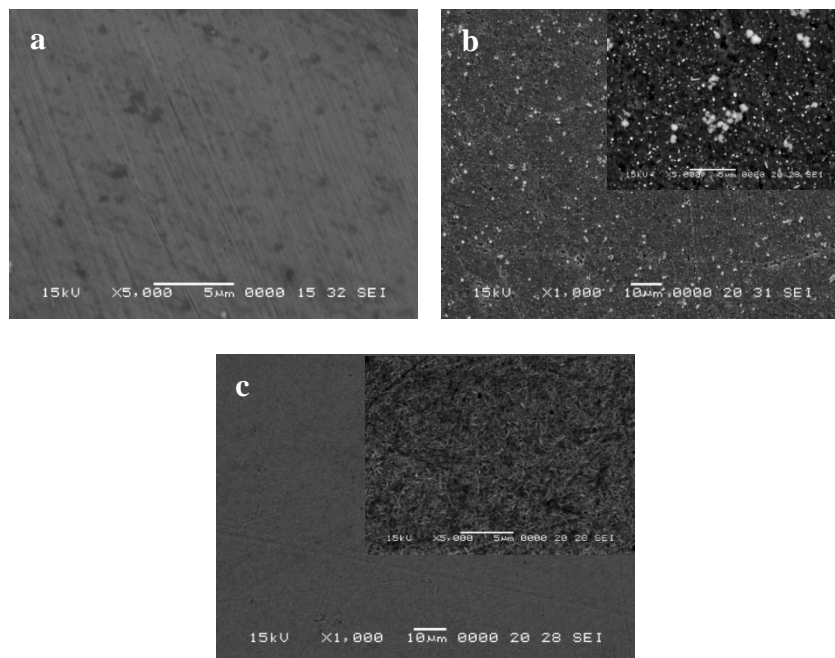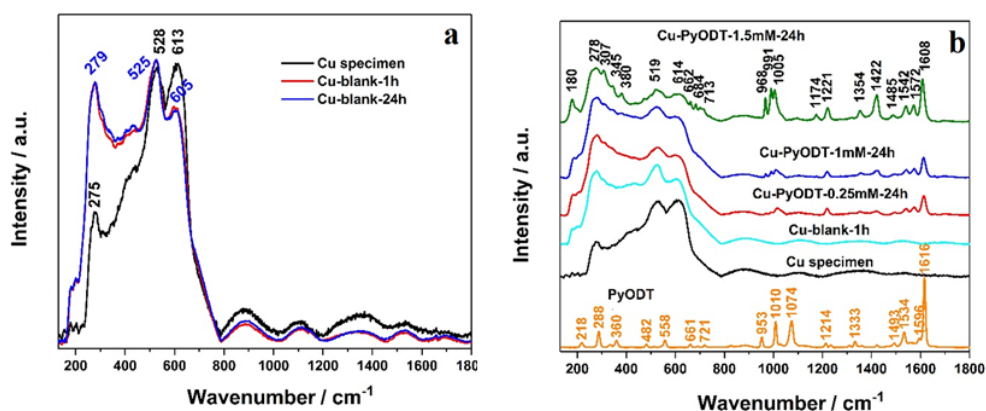

Figure 6. SEM micrographs of the copper surface before (a) and after 24 h of immersion in 3.5 wt.% NaCl solution in the absence (b) and in the presence of 1 mM PyODT (c).
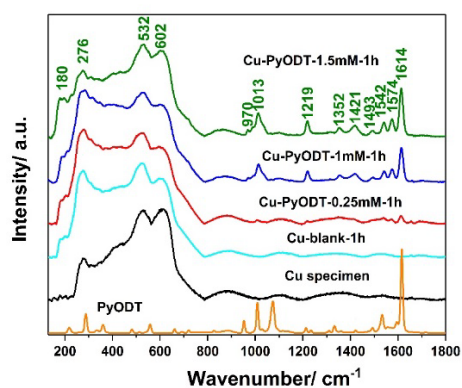
Figure 7. EDX analysis of the copper surface after 24 h immersion in 3.5 wt.% NaCl solution in the absence (a) and in the presence of 1 mM PyODT (b).


Figure 8. Raman spectra of the copper surface before and after immersion in 3.5 wt.% NaCl solution in the absence (blank, (a)), and in the presence of 1 and 1.5 mM of PyODT for 24 h (b). PyODT structure in the solid state (thione form) and after addition on the copper surface (c).


Figure 9. Raman spectra of the copper surface after 1 hour of immersion in 3.5 wt.% NaCl in the absence (blank) and the presence of 0.25, 1 and 1.5 mM of PyODT. Raman spectra of PyODT (solid state) and of Cu specimen are included for comparison.

41
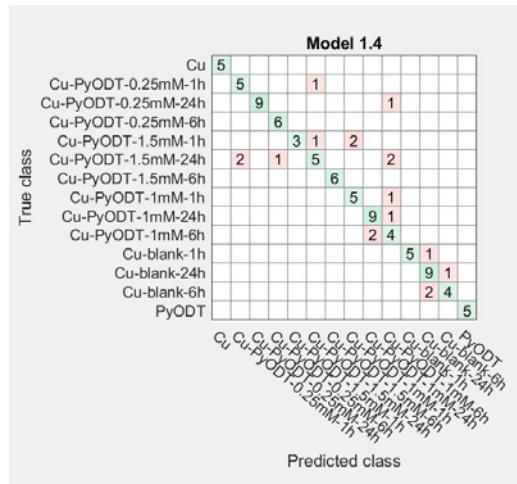
Figure 10. Confusion matrix for classification of the investigated copper electrodes using machine learning algorithms applied to Raman spectra (copper specimen and the anti-corrosion agent, PyODT, have been also added).
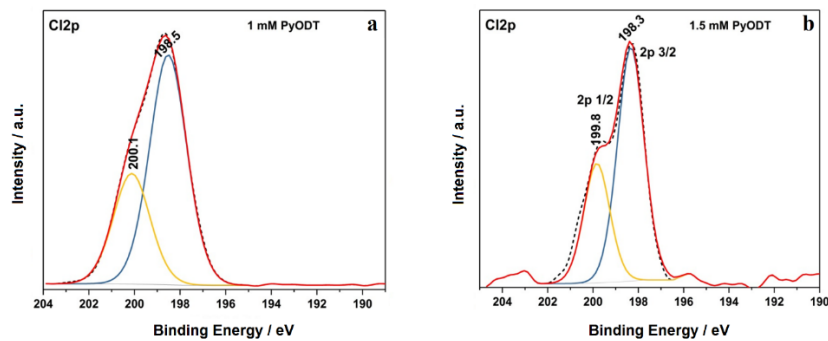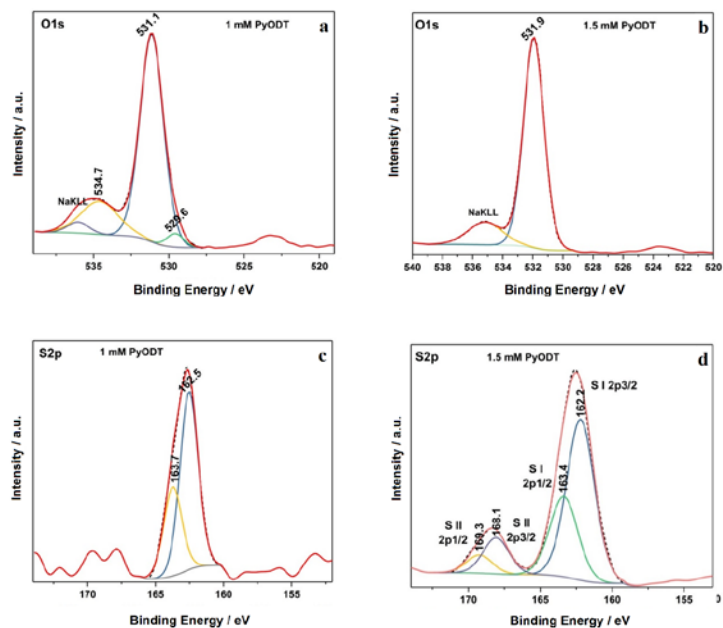

Figure 11. Cl2p XPS spectra of copper electrode after 24 h of immersion in 3.5 wt.% NaCl solution containing: a) 1mM, and b) 1.5 mM PyODT.
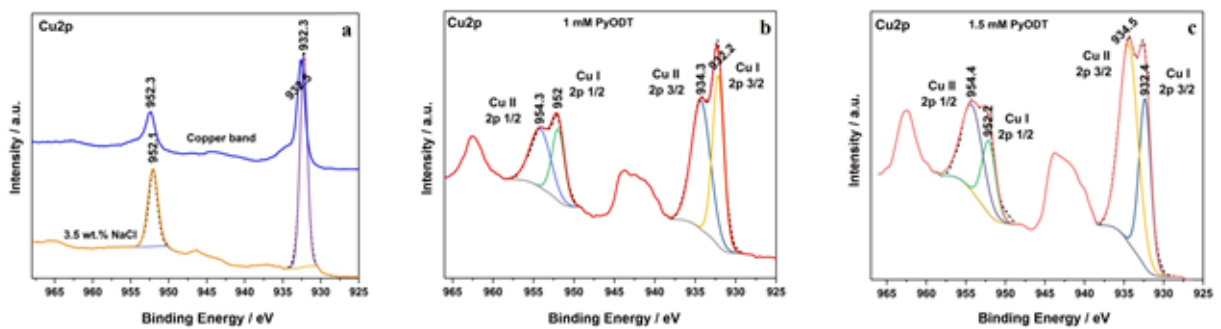
Figure 12. Cu2p XPS spectra of copper electrode before (a) and after 24 h of immersion in 3.5 wt.% NaCl solution containing either 1 mM PyODT (b) or 1.5 mM PyODT (c).
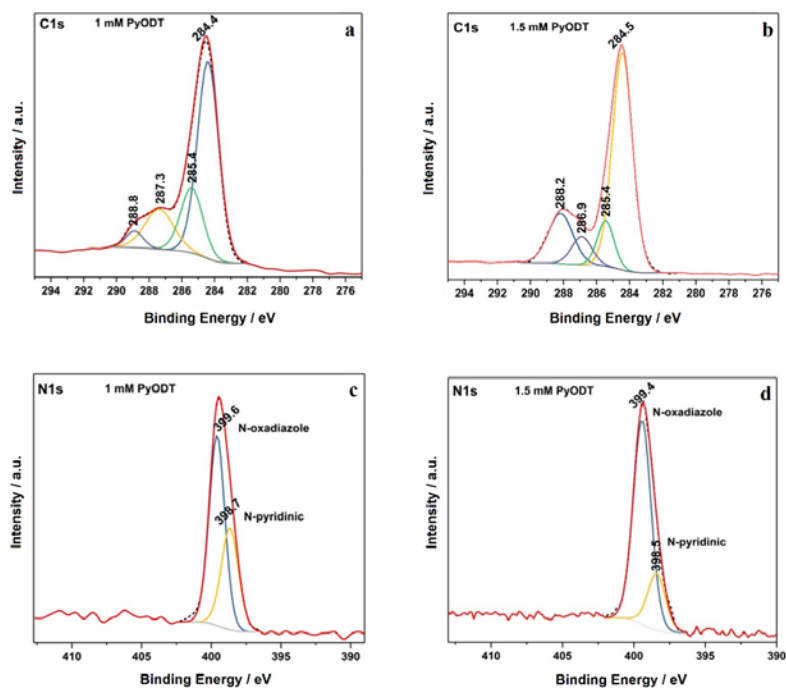
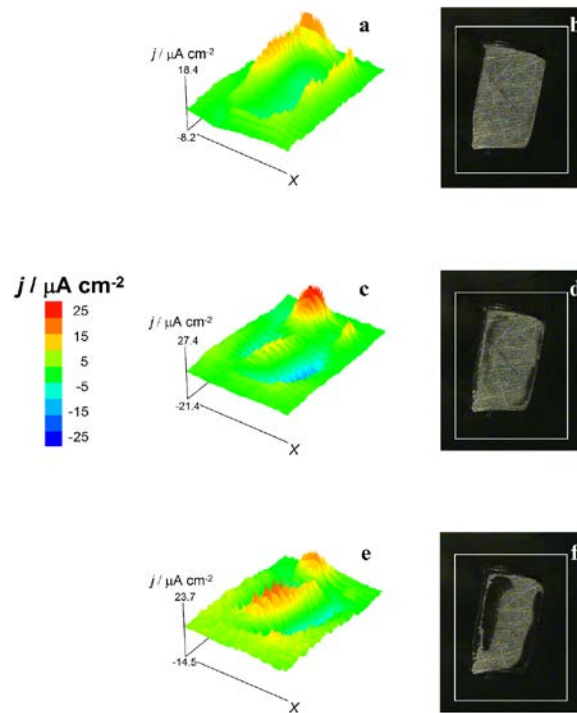**Figure 13.** C1s (a, b) and N1s (c, d) XPS spectra of copper electrode after 24 h of immersion in 3.5 wt.% NaCl solution containing either 1 mM PyODT (a, c) or 1.5 mM PyODT (b, d).


Figure 14. O1s (a, b) and S2p (c, d) XPS spectra of copper electrode after 24 h of immersion in 3.5 wt.% NaCl solution containing either 1 mM PyODT (a, c) or 1.5 mM PyODT (b, d).

Figure 15. SVET maps (a,c,e) and optical images (b,d,f) of Cu exposed to 50 mM NaCl for 20 (a,b), 60 (c,d,), and 164 min (e,f). SVET scan size: 1700 µm × 2430 µm. Grid: 41 × 41 data-points acquisition. Scan duration: 15 min. The white rectangles drawn on the optical micrographs correspond to the scanned area.
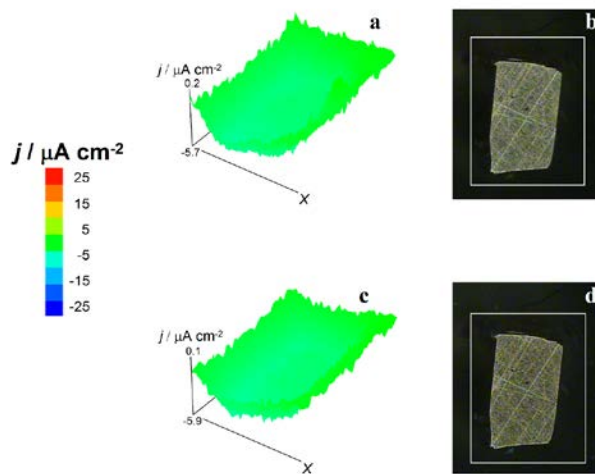
Figure 16. SVET maps (a,c) and optical images (b,d) of Cu exposed to 50 mM NaCl containing 1.5 mM of PyODT for (a,b) 20, and (c,d) 146 min. SVET scan size: 1720 µm × 2390 µm. Grid: 41 × 41 data-points acquisition. Scan duration: 15 min. The white rectangles drawn on the optical micrographs correspond to the scanned area.
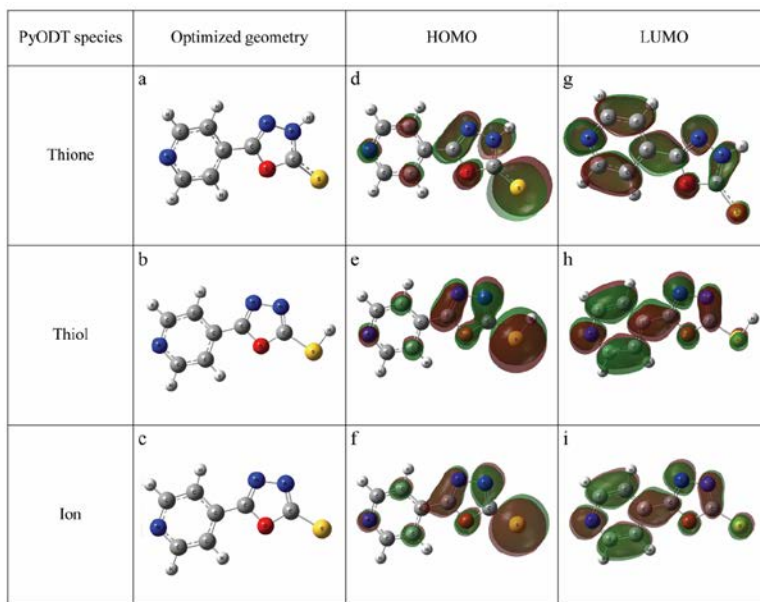
Figure 17. (a-c) Optimized molecular structures, and electron density distributions of (d-f) HOMO and (g-h) LUMO levels in all the forms of the PyODT inhibitor. They were obtained using the B3LYP/6-311++G(d,p) level of theory in solution at the presence of water as solvent by applying the CPCM model.
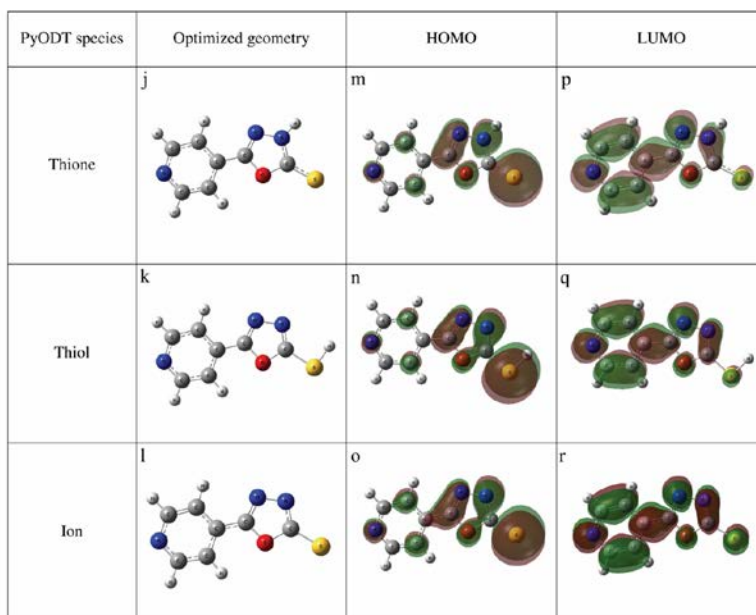
Figure 18. (j-l) Optimized molecular structures of all forms of the PyODT inhibitor, and electron density distributions of the (m-o) HOMO and (p-r) LUMO orbitals determined using B3LYP/6-311++G(d,p) level of theory in the gas phase.
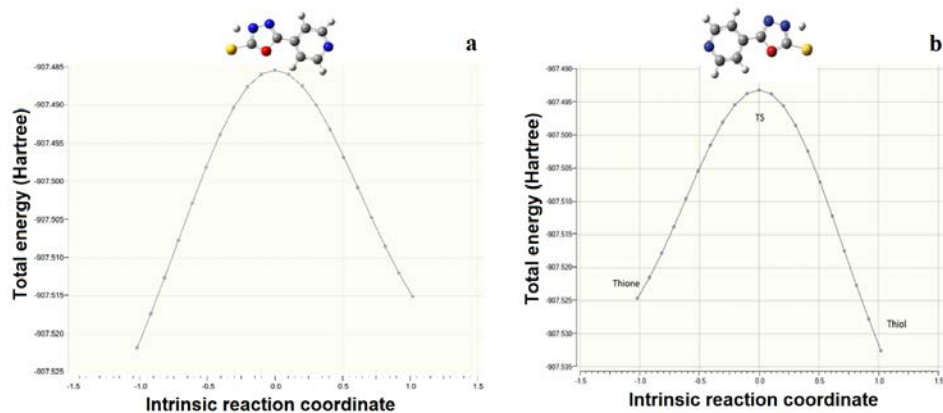
Figure 19. Prototrophic thione-thiol tautomerism energy profiles of the PyODT inhibitor computed under DFT/B3LYP/6-311 G(d,p) level of theory using QST2 method: a) in the gas phase, and b) in aqueous solution.
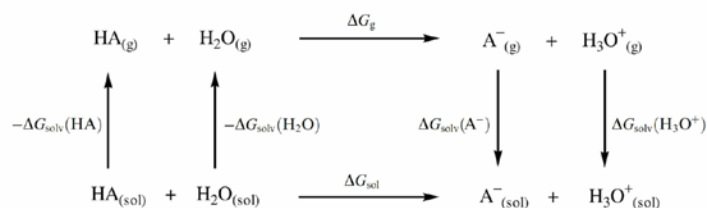
$$\Delta G_{sol} = \Delta G_g + \Delta G_{solv}(A^-) + \Delta G_{solv}(H_3O^+)$$
$$- \Delta G_{solv}(HA) - \Delta G_{solv}(H_2O),$$

$$pK_a = \frac{\Delta G_{sol}}{1.364} - \log[H_2O]$$

Figure 20. Thermodynamic cycle and related equations used in the calculation of pK_a.

Copper atom   Chloride ion   Sodium ion   Water molecule
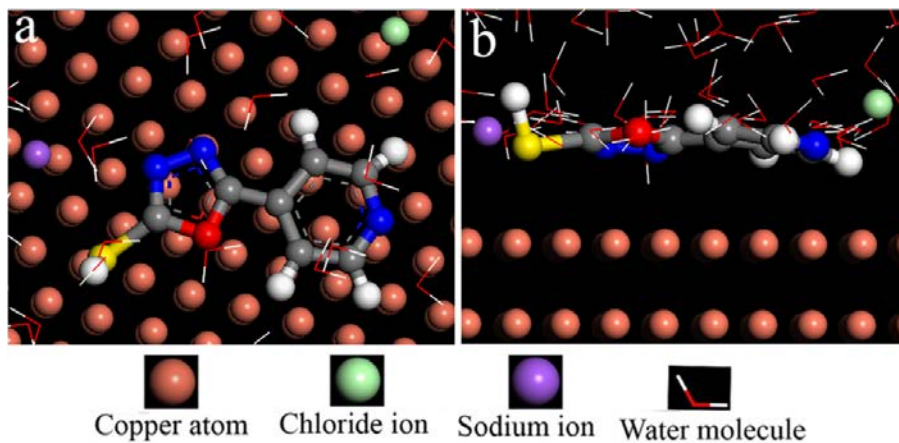
Figure 21. (a) Top and (b) side views of the equilibrium adsorption configurations of PyODT molecules on Cu (111) surfaces at 298 K obtained from MD simulations.

Table 1. Impedance parameters of copper in 3.5wt.% NaCl solution without and with various concentrations of PyODT, determined at different immersion times.

Time / h	R_f / kΩ cm²	CPE_f / μF s^{n-1} cm^{-2}	n_f	C_f / μF cm^{-2}	R_{ct} / kΩ cm²	CPE_{dl} / μF s^{n-1} cm^{-2}	n_{dl}	C_{dl} / μF cm^{-2}	W / S s$^{1/2}$ cm^{-2}	η_{imp} (%)
					Blank					
1	0.52	42.5	0.817	18.03	3.60	283.60	0.516	289.10	0.0013	-
4	0.89	70.8	0.787	33.47	3.48	272.50	0.531	260.30	0.0017	-
8	2.19	80.8	0.773	48.57	3.54	145.00	0.535	81.10	0.0017	-
12	2.80	86.5	0.768	56.36	6.36	59.00	0.500	22.14	0.0021	-
24	2.89	94.0	0.782	65.33	8.03	39.20	0.500	12.33	-	-
48	5.12	77.5	0.800	34.59	6.37	42.90	0.716	25.69	0.0035	-
72	0.14	85.1	0.806	29.49	5.83	58.70	0.714	38.21	0.0037	-
168	0.08	87.6	0.833	32.18	4.68	141.00	0.673	115.20	-	-
					0.5 mM PyODT					
1	0.82	50.4	0.721	14.7	7.35	137.00	0.616	137.60	7.3E-4	51.1
4	1.57	32.5	0.750	12.05	7.89	92.50	0.652	78.11	3.9E-4	55.8
8	3.56	0.68	0.905	0.36	26.75	60.24	0.534	91.43	4.1E-4	86.8
12	14.07	0.61	0.900	0.36	45.98	18.04	0.642	16.25	8.8E-5	86.2
24	22.04	0.47	0.911	0.30	103.30	4.14	0.394	1.16	7.6E-5	92.2
48	20.12	0.50	0.894	0.29	103.10	4.31	0.520	2.04	5.9E-5	93.8
72	18.84	0.59	0.877	0.31	76.72	14.24	0.454	15.85	1.5E-4	92.4
168	0.026	1.86	0.863	0.38	7.12	78.06	0.756	64.61	0.00117	34.3
					1 mM PyODT					
1	1.20	4.32	0.927	2.86	50.35	36.01	0.502	64.98	-	92.8
4	69.58	0.80	0.919	0.63	100.60	9.88	0.512	9.83		96.5
8	116.20	0.80	0.913	0.64	156.80	4.12	0.476	2.54	-	97.7
12	198.60	0.81	0.930	0.71	298.90	5.64	0.502	9.45	-	98.1
24	273.50	0.66	0.930	0.58	417.40	4.64	0.510	8.74	-	98.1
48	355.0	0.62	0.923	0.55	555.50	5.23	0.500	15.21	-	98.9
72	460.50	0.59	0.925	0.53	642.80	5.19	0.512	16.36	-	99.1
168	545.30	0.55	0.922	0.49	647.50	6.24	0.512	23.64	-	99.3
					1.5 mM PyODT					
1	28.19	0.82	0.914	0.57	53.86	27.63	0.417	48.19	-	93.3
4	71.25	1.39	0.933	1.18	188.40	5.55	0.457	5.86		98.2
8	135.00	0.61	0.918	0.49	305.00	5.17	0.454	8.93	-	98.8
12	181.34	0.69	0.926	0.59	513.80	2.46	0.443	3.30	-	98.8
24	288.00	0.60	0.912	0.51	1224.00	1.82	0.500	4.06	-	99.3
48	402.90	0.54	0.919	0.47	1624.00	1.35	0.471	3.28	-	99.6
72	531.90	0.45	0.916	0.40	2005.00	1.86	0.545	5.55	-	99.7
168	595.00	0.40	0.918	0.35	2055.00	1.23	0.550	2.63	-	99.8

Table 2. Corrosion parameters of copper in 3.5wt.% NaCl solution, in the absence and in the presence of various concentrations of PyODT, determined at different exposure times from the polarization curves in Figure 5.

[PyODT] / mM	E_{corr} / mV vs. Ag/AgCl/KCl$_{sat}$	j_{corr} / μA cm^{-2}	β_a / mV dec^{-1}	η_{Pol} (%)
1-h immersion				
0	- 206.6	131.5	64.2	0
0.25	-191.1	11.7	56.2	11.3
0.5	-173.6	43.4	72.0	67.0
1.0	-209.7	1.7	110.9	98.7
1.5	-198.65	1.0	530.2	99.2
48-h immersion				
0	-177.8	161.5	57.1	-
0.25	-172.6	397.4	60.7	-146.1
0.5	-180.1	1.8	56.9	98.9
1	-122.9	1.1	229.7	99.3
1.5	-12.6	0.5	232.0	99.7

Table 3. Results obtained after verifying the prediction model 1.4 – Linear Discriminant (accuracy 81.6%) on the testing set.

True class	Predicted class
Cu	Cu
Cu	Cu
Cu	Cu
Cu	Cu
PyODT	PyODT
Cu-blank-1h	Cu-blank-1h
Cu-blank-1h	Cu-blank-1h
Cu-blank-6h	*Cu-blank-24h*
Cu-blank-6h	Cu-blank-6h
Cu-blank-24h	Cu-blank-24h
Cu-blank-24h	Cu-blank-24h
Cu-PyODT-0.25mM-1h	Cu-PyODT-0.25mM-1h
Cu-PyODT-0.25mM-6h	Cu-PyODT-0.25mM-6h
Cu-PyODT-0.25mM-6h	Cu-PyODT-0.25mM-6h
Cu-PyODT-0.25-6h	Cu-PyODT-0.25mM-6h
Cu-PyODT-0.25mM-24h	Cu-PyODT-0.25mM-24h
Cu-PyODT-0.25mM-24h	Cu-PyODT-0.25mM-24h
Cu-PyODT-1mM-1h	Cu-PyODT-1mM-1h
Cu-PyODT-1mM-1h	Cu-PyODT-1mM-1h
Cu-PyODT-1mM-1h	Cu-PyODT-1mM-1h
Cu-PyODT-1mM-1h	Cu-PyODT-1mM-1h
Cu-PyODT-1mM-6h	Cu-PyODT-1mM-6h
Cu-PyODT-1mM-6h	Cu-PyODT-1mM-6h
Cu-PyODT-1mM-6h	Cu-PyODT-1mM-6h
Cu-PyODT-1mM-6h	Cu-PyODT-1mM-6h
Cu-PyODT-1mM-24h	Cu-PyODT-1mM-24h
Cu-PyODT-1mM-24h	Cu-PyODT-1mM-24h
Cu-PyODT-1mM-24h	Cu-PyODT-1mM-24h
Cu-PyODT-1mM-24h	Cu-PyODT-1mM-24h
Cu-PyODT-1mM-24h	Cu-PyODT-1mM-24h
Cu-PyODT-1mM-24h	Cu-PyODT-1mM-24h
Cu-PyODT-1mM-24h	Cu-PyODT-1mM-24h
Cu-PyODT-1mM-24h	Cu-PyODT-1mM-24h
Cu-PyODT-1.5mM-1h	Cu-PyODT-1.5mM-1h
Cu-PyODT-1.5mM-6h	Cu-PyODT-1.5mM-6h
Cu-PyODT-1.5mM-24h	Cu-PyODT-1.5mM-24h
Cu-PyODT-1.5mM-24h	Cu-PyODT-1.5mM-24h
Cu-PyODT-1.5mM-24h	Cu-PyODT-1.5mM-24h

Table 4. Selected structural parameters of optimized geometry for all forms of the PyODT molecule using B3LYP/6-311++G(d,p) level of theory in gas phase and in solution at the presence of water as solvent by applying CPCM model.

phase	species	r_{C2-S6}	r_{C2-N3}	r_{C2-O1}	$<_{N3-C2-O1}$	$\Pi_{O1-C2-S6-C5}$	$\Pi_{C9-C8-C5-O1}$
gas	Thione	1.6371	1.3595	1.3842	102.8515	180.0272	180.094
	Thiol	1.7499	1.2945	1.3566	113.19	180.0265	-0.0165
	Ion	1.6856	1.337	1.404	108.4724	180.0118	0.0034
solution	Thione	1.6542	1.3481	1.3732	103.7294	180.0028	-0.0253
	Thiol	1.7465	1.2981	1.3544	112.7358	179.9808	0.0059
	Ion	1.7049	1.3217	1.3914	109.2307	179.9995	0.0343

See equation (5) for the numbering of the atoms. Bond distances, r, in Å; bond angles, $<$, and dihedral angles, Π, in degrees.

Table 5. Quantum chemical parameters for thione and thiol tautomers as well as the thiolate ion of PyODT calculated using the B3LYP/6-311++G(d,p) level of theory in gas phase and in solution at the presence of water as solvent by applying the CPCM model.

Parameters	Thione		Thiol		Thiolate ion	
	gas phase	solution	gas phase	solution	gas phase	solution
$E(RB3LYP)$ / a.u.	-907.5591	-907.5724	-907.5424	-907.5540	-907.0355	-907.1188
E_{HOMO} / eV	-7.2119	-7.2013	-7.2603	-7.2600	-6.9781	-6.9917
E_{LUMO} / eV	-5.1473	-5.1571	-5.1601	-5.1615	-5.1707	-5.1492
ΔE	2.0645	2.0441	2.1002	2.0986	1.8074	1.8425
μ / D	2.6629	4.0308	2.5831	3.7211	8.4076	12.8869
ΔN	0.54	0.54	0.53	0.53	0.55	0.55

Table 6. Computational data used for the calculation of pK_a for thione and thiol tautomers of the PyODT inhibitor using B3LYP/6-311++G(d,p) level of theory in gas phase and in solution at the presence of water as solvent by applying CPCM model.

Species	G_g^0(Hartree/particle)	G_{sol}^0(Hartree/particle)	ΔG^0 / kcal mol^{-1}	ΔG_{gas} / kcal mol^{-1}	ΔG_{sol} / kcal mol^{-1}	pK_a
Thion	-907.477279	-907.490514	-8.30509485	0.249354	0.011998269	3.77
Thion^{-1}	-906.966722	-907.049792	-52.1272557			
Thiol	-907.464833	-907.476604	-7.38642021	0.236908	-1.19963047	-2.62
Thiol^{-1}	-906.966722	-907.049792	-52.1272557			
H_2O	-76.454891	-76.462985	-5.07906594			
H_3O^+	-76.716094	-76.839482	-77.4272039			

$R = 1.987$ kcal mol^{-1} K^{-1}; $T = 298.15$ K; log [H_2O] = 1.744293
$\Delta G_{sol}(H_3O^+) = 110.2$ kcal mol^{-1} (experimental) [97]

49

Table 7. Interaction and binding energies obtained from MD simulations for the adsorption of PyODT on Cu (111) surface at 298 K.

System	$E_{adsorption}$ / kJ mol^{-1}	$E_{binding}$ / kJ mol^{-1}
Cu (111) + PyODT	-211.12	211.12